

Decoding X-ray observations from centres of galaxy clusters using MCMC

Kiran Lakhchaura^{1*}, Tarun Deep Saini^{1†} and Prateek Sharma^{1‡}

¹ Department of Physics, Indian Institute of Science, Bangalore 560012, India

16 July 2018

ABSTRACT

Traditionally the thermodynamic profiles (gas density, temperature, etc.) of galaxy clusters are obtained by assuming spherical symmetry and modeling projected X-ray spectra in each annulus. The outer annuli contribute to the inner ones and their contribution needs to be subtracted to obtain the temperature and density of spherical shells. The usual deprojection methods lead to propagation of errors from outside to in and typically do not model the covariance of parameters in different radial shells. In this paper we describe a method based on a free-form model of clusters with cluster parameters (density, temperature) given in spherical shells, which we *jointly* forward fit to the X-ray data by constructing a Bayesian posterior probability distribution that we sample using the MCMC technique. By systematically marginalising over the nuisance outer shells, we estimate the inner entropy profiles of clusters and fit them to various models for a sample of Chandra X-ray observations of 17 clusters. We show that the entropy profiles in almost all of our clusters are best described as cored power laws. A small subsample is found to be either consistent with a power law, or alternatively their cores are not fully resolved (smaller than, or about few kpc). We find marginal evidence for bimodality in the central values of entropy (and cooling time) corresponding to cool-core and non cool-core clusters. The minimum value of the ratio of the cooling time and the free-fall time ($\min[t_{\text{cool}}/t_{\text{ff}}]$; correlation is much weaker with core entropy) is anti-correlated with $H\alpha$ and radio luminosity. $H\alpha$ emitting cold gas is absent in our clusters with $\min(t_{\text{cool}}/t_{\text{ff}}) \gtrsim 10$. Our lowest core entropies are systematically and substantially lower than the values quoted by the ACCEPT sample.

Key words: X-rays: galaxies: clusters – galaxies: clusters: intracluster medium – methods: statistical

1 INTRODUCTION

Observations of large scale distribution of galaxies (e.g., Colless et al. 2001) and numerical simulations of gravitational structure formation (e.g., Davis et al. 1985) show that the mass in the Universe is distributed in the form of a cosmic foam, with pancakes, filaments, voids, and groups and clusters. Galaxy clusters, which form at the intersections of massive cosmological filaments, are the most massive, spherical, virialized objects in the Universe. Galaxy clusters, containing up to 1000s of mostly red galaxies, lie at the exponential end of the halo mass distribution, and hence their abundance is a sensitive function of cosmological parameters such as the

amplitude of perturbations at recombination and the cosmological matter fraction (e.g., Eke et al. 1996; see Allen et al. 2011 for a recent review).

Galaxy cluster observations also shed light on galaxy formation, in particular the role of the extended hot halo gas, which is left behind as a consequence of galaxy formation (White & Rees 1978). Unlike galaxy clusters in which the hot gas density is high, the hot gas halo is very difficult to observe in lower mass halos. However, it is present, and is expected to be spread out beyond the viral radius, accounting for most of the galactic ‘missing’ baryons (e.g., Anderson & Bregman 2010; Sharma et al. 2012b). The diffuse hot halo is also a reservoir from which the cold gas needed for ongoing star formation is accreted, and into which metals due to supernovae are deposited (see Putman et al. 2012 for a review).

The galaxy cluster core, where the cooling time of the

* E-mail : kiru11184@gmail.com

† E-mail : tarun@physics.iisc.ernet.in

‡ E-mail : prateek@physics.iisc.ernet.in

hot gas is shorter than the Hubble time, is most interesting from the perspective of galaxy formation. Observations show that cluster cores exist in at least two states: cool-cores (CC) and non-cool-cores (NCC). Cool cores have short ($\lesssim 1$ Gyr) cooling times (e.g., Croston et al. 2008; Cavagnolo et al. 2009; Hudson et al. 2010) and non cool-cores have long cooling times ($\gtrsim 1$ Gyr). Some authors also talk about intermediate or weak cool-core clusters (e.g., Santos et al. 2008; Rossetti & Molendi 2010). There is some merit in studying the entropy of hot gas because (at least in simple 1-D models; this breaks down in 2/3-D as mixing, condensation and dropout have a non-trivial impact on hot gas entropy) it only changes at the virial shock and in the central cooling/heating regions (e.g., Tozzi & Norman 2001; Voit et al. 2003). The core entropy is also a measure of preheating of the intergalactic medium (IGM) at the epoch when the central gas was accreted into dark matter halos (e.g., Kaiser et al. 1991).

There is disagreement in the literature on the nature of entropy profiles in cluster cores. The extreme views being that all clusters have constant entropy cores (Cavagnolo et al. 2009; $K \equiv T_{\text{keV}}/n_e^{2/3} = K_0$ at smallest radii; T_{keV} is the temperature in keV and n_e is the electron number density) and all centres have power law entropy profiles (we call them cusps, $K \propto r^{\alpha_1}$ at smallest radii; Panagoulia et al. 2014). Of course, latter is a more general form and includes former as a special case ($\alpha_1 = 0$). The slope of the entropy/density profile in the core constrains the models of active galactic nucleus (AGN) feedback in cluster cores. For example, a decreasing entropy towards the centre implies that the Bondi accretion rate onto the black hole is higher; similar conditions may also lead to (the more plausible) cold feedback (Pizzolato & Soker 2005), triggered when the ratio of the cooling time and the free-fall time ($t_{\text{cool}}/t_{\text{ff}}$; $t_{\text{cool}} \equiv 1.5p/[n_e n_i \Lambda]$, where p is gas pressure, n_e/n_i is electron/ion number density and Λ is the temperature-dependent cooling function; $t_{\text{ff}} \equiv (2r/g)^{1/2}$ is the local free-fall time) becomes $\lesssim 10$ (Sharma et al. 2012a; Gaspari et al. 2013). Also, there are predictions from numerical simulations for the hot gas entropy profile; e.g., Prasad et al. (2015) suggest that the entropy profile for lower core entropy is steeper at ~ 10 kpc scales (top-left panel of their Fig. 11; middle panel of our Fig. 7 shows some evidence for this). Some papers have argued that $t_{\text{cool}}/t_{\text{ff}}$ (McCourt et al. 2012; Sharma et al. 2012a; Voit et al. 2015) is the physical parameter that delineates hot gas halos in which cold gas condensation, star-formation and AGN activity occur from those in which they are absent. Such theoretical predictions can be tested by appropriately analyzing the X-ray data from cluster cores and by comparing with cold gas and radio observations.

Since the clusters are seen in projection, to reconstruct the three dimensional thermodynamic profiles of a cluster requires deprojection of data. To keep the reconstruction bias free, a free-form model of the cluster (that allows n_e and T to vary arbitrarily with radius) is preferred in comparison to analytical fits. The cluster can be divided into N spherical shells that are seen in projection as N annuli. The number density and temperature in the shells are the $2N$ parameters of the free-form fit to the cluster (we also try some models in which the shell elemental abundance is kept as a free parameter; see Appendix A). The inverse method

(e.g., Russell, Sanders, & Fabian 2008) employs the elegant idea that since the last radial annulus draws photons only from the last shell, the last shell parameters can be obtained directly. Then subtracting the contribution of the last shell from the next inner shell, one can sequentially obtain the parameters of each shell. The number of parameters fitted at any step is just two (three if elemental abundance is allowed to vary in shells), so this method is very efficient. Although this method works well for most cases, one downside of this method is that the errors in the parameters are not calculated jointly for all shells. For example, outer shell spectra affect the density and temperature of inner shells but not vice versa. Oscillations in deprojected temperature sometimes seen due to poor quality X-ray spectra may be manifestations of biased temperatures estimated in outer shells affecting the inner shells.

To avoid this, in this paper, we *jointly fit the parameters of all the shells to the cluster data through forward fitting*. This increases the number of parameters considerably. We construct the Bayesian posterior probability distribution function for the $2N$ parameters of a cluster. To sample the posterior probability distribution, we use Markov Chain Monte Carlo (MCMC) method and extract the most likely density, temperature, entropy, etc. profiles in cluster cores and their (co)variances. We call our method jMCMC ('j' stands for the joint fitting of all shell parameters). Since the central thermodynamic profiles for clusters are the most interesting for studying cooling and star formation in clusters, we marginalize over model parameters at outer radii to obtain much more precise estimates in the core ($R \sim 10$ kpc).

Like all such models, we make the assumption that the X-ray emitting gas is spherically symmetric. This is manifestly a simplification as most cool-core clusters (which are generally more relaxed) show X-ray cavities and radio bubbles (see McNamara & Nulsen 2007 for a review). Quantifying systematic bias introduced due to the assumption of spherical symmetry is left for future.

We present our method and its tests in section 2; some tests to optimize our method on the test cluster are shown in Appendix A. Section 3 presents our sample and results from from fitting flat core entropy profiles. Single and double power law profiles are presented in Appendix B & C. Readers not interested in technical details may directly proceed to section 4 in which we discuss astrophysical implications of our results. We conclude in section 5.

2 METHOD

The X-ray data comprise photon counts at a position on the sky as a function of frequency. We divide the projected counts into N annuli and M spectral channels. The number of spectral channels are chosen to ensure that each channel gets a minimum of 25 counts to ensure Gaussian statistics for the photon noise. We define the radius R_i of an annulus as the distance from the centre of the cluster to the centre of the annulus. The three dimensional spherical shells are assigned the same radii as the annuli. The annulus/shell number increases from the centre outwards. The observed counts in the i^{th} annulus is given by

$$\mathbf{C}_{iJ} = \mathbf{D}_{iJ} - \mathbf{B}_{iJ}. \quad (1)$$

In our notation the lower case Roman letters denote the annuli and the upper case Roman letters denote the spectral bins. The quantities \mathbf{D}_{iJ} and \mathbf{B}_{iJ} are the counts detected in the spectrum in the J^{th} spectral bin of the i^{th} annulus of the source, and the corresponding weighted spectrum from the blank sky observation, respectively.

The photon count (\mathbf{C}_{iJ}) in each annulus is a sum of contributions from different spherical shells of radius larger than that of the particular annulus. Since the outermost annulus receives photons only from the last shell, its photon count can be taken to be the projected photon count of the outermost shell. The standard deprojection technique relies on removing the spectral contributions of the outer shells from the given annulus with the appropriate volume factors to obtain the photon count of the shell. The procedure is then applied iteratively to the inner annuli to obtain the count rates corresponding to individual shells. The individual shells can then be fitted to obtain the gas number density n_i and temperature T_i in the i^{th} shell.

Since in this method the errors in the photon-count in the outer shells systematically propagate inward, the resulting individual shell counts are actually correlated with each other. However, it is difficult to take this correlation into account, since every i^{th} shell spectrum is fitted individually for n_i and T_i , and not collectively as \mathbf{n}, \mathbf{T} , where \mathbf{n} and \mathbf{T} are the N -dimensional density and temperature vectors. The usual practice is to use Monte Carlo methods to estimate the range of n and T in each shell allowed by the data.

Since we are primarily interested in the central regions of galaxy clusters, it is useful to be able to systematically isolate the inner shells by statistically marginalising over the outer shells to obtain the best possible estimate for the inner shells (the choice of inner shells is described in section 2.1). For this we first need to construct the likelihood function for data based on the free-form model \mathbf{n}, \mathbf{T} . Then using Bayesian statistics, we can construct the posterior probability for the model parameters.

To construct the probability distribution function for the unknown parameters of the shell n_i, T_i , we begin with the expression for the *model* of the counts for each annulus through

$$\mathbf{M}_{iJ} = \sum_{k=i}^N \sum_E \dot{\mathbf{C}}^{\text{th}}(n_k, T_k, E) R_k(E, J) A_k(E) V_{\text{proj}}(i, k) \Delta t, \quad (2)$$

where $\dot{\mathbf{C}}^{\text{th}}(n_k, T_k, E)$ is the model photon count flux for the k^{th} shell at energy E per unit time per unit source volume for gas density n_k and temperature T_k . $\dot{\mathbf{C}}^{\text{th}}$ is calculated using the *wabs* photoelectric absorption model (Morrison & McCammon 1983) and the Astrophysical Plasma Emission Code (*apc*; Smith et al. 2001) in the X-ray spectral analysis package (XSPEC; see Arnaud 1996). We have used Xspec Version 12.8.2 and Atomdb version 2.0.2 for all our analysis. The solar elemental abundance tables used for the *apc* model are from Anders & Grevesse (1989) and those for the *wabs* model are from Anders & Ebihara (1982). The redshift (z), elemental abundance (Z) and neutral hydrogen column density along the source direction (N_H), are assumed to be constant (in section A we show that fixing the elemental abundance across shells does not affect our density and temperature determination). $R_k(E, J)$ is the probability of a

photon with energy E to be detected in the detector channel J , and $A_k(E)$ is the effective area of the detector at energy E for the k^{th} annulus. $V_{\text{proj}}(i, k)$ is the projected volume of the k^{th} shell intercepted by the i^{th} annulus ($k \geq i$), and Δt is the exposure time of the observation.

$$V_{\text{proj}}(i, k) = V(i, k+1) - V(i+1, k+1) - V(i, k) + V(i+1, k), \quad (3)$$

where $V(i, k) = (4\pi/3)(R_{ko}^2 - R_{ii}^2)^{3/2}$, R_{ii} and R_{ko} being the inner and outer radii of the i^{th} and k^{th} shells, respectively (see Kriss, Cioffi, & Canizares 1983).

In terms of the model parameters \mathbf{n}, \mathbf{T} , the χ^2 is given by

$$\chi^2(\mathbf{n}, \mathbf{T}) = \sum_{i=1}^N \sum_J \left(\frac{\mathbf{C}_{iJ} - \mathbf{M}_{iJ}}{\sigma_{iJ}} \right)^2 \quad (4)$$

where $\sigma_{iJ} = \sqrt{\mathbf{D}_{iJ} + \mathbf{B}_{iJ}}$ is the Poisson error in the counts in the J^{th} channel of the i^{th} annulus in the source observation. In this expression the summation over J matches the observed spectrum for the i^{th} annulus, and the summation over i gives the combined match for the full data across all radial bins. The Bayesian posterior probability distribution function (PDF) of the model is then given by

$$P(\mathbf{n}, \mathbf{T} | \mathbf{D}) \propto \exp \left(-\frac{\chi^2(\mathbf{n}, \mathbf{T})}{2} \right) P(\mathbf{n}, \mathbf{T}), \quad (5)$$

where $P(\mathbf{n}, \mathbf{T})$ is the prior PDF for the model parameters. Since we *jointly* fit all shell parameters and use MCMC to sample the PDF, we call our approach joint-MCMC or jMCMC.

2.1 MCMC method

We are specifically interested in the behaviour of entropy close to the centre of galaxy clusters, therefore we divide the radial bins roughly into central and outer parts, and marginalise over the parameters of the outer part. The observed entropy profiles show departure from single power law (straight line in a log-log plot) both at small and large radii. We retain all the annuli in the interior of a cluster until the annulus beyond which they depart from a power law and treat them as the inner region, which we fit to various entropy models (eqs. 10-12).

Given the large number of radial bins, it is hard to use eq. 5 directly, since marginalisation through direct integration of parameters of the outer part of the cluster is computationally expensive. A popular method for marginalising is the Markov-Chain Monte Carlo (MCMC) technique using the Metropolis-Hastings algorithm (Metropolis et al. 1953; Hastings 1970). This method employs a random walk through the parameter space while maintaining the condition of detailed balance (see, e.g., Press et al. 2003, for details). After some burn-in steps that are discarded, the random walk starts sampling the underlying PDF, so the parameter values from the random walk behave as if they were drawn from the PDF. The random walk produces a chain of points in the parameter space $\mathbf{n}_\tau, \mathbf{T}_\tau$, where τ denotes the order in the chain. These samples (chains), being drawn from the target PDF (eq. 5), can be used to compute various integrals over the PDF. From the chain in the parameter

space, we estimate the parameters n_i, T_i for the i^{th} shell by computing the sample means (\bar{n}_i, \bar{T}_i) . For example

$$\bar{n}_i = \frac{1}{N_s} \sum_{\tau=1}^{N_s} n_{i\tau},$$

where N_s is the number of samples. Similarly, (co)variances between the shell parameters can also be calculated.

2.1.1 Implementing MCMC

The calculation of model \mathbf{M}_{iJ} using XSPEC makes the MCMC runs slow. Fortunately, for most clusters n and T fall into a well-known narrow range. Our prior probability function $P(\mathbf{n}, \mathbf{T})$ (eq. 5) is chosen to be uniform in the box defined by $0.0001 < n_i < 1$ and $0.1 < T_i < 15$, where the units of n and T are cm^{-3} and keV , respectively. The number density n is divided into 500 logarithmic intervals, and T is divided into 150 linear intervals. The grid size for \mathbf{n}, \mathbf{T} is much smaller than the typical error bars on the parameter values. We pre-calculate the template of $\dot{\mathbf{C}}^{\text{th}}$ on this grid.

We use Metropolis-Hastings sampling along one parameter at a time for generating chains, so the random walk is constructed by updating individual parameters sequentially. The proposal density along any single parameter being updated is chosen to be Gaussian

$$q(x) = \frac{1}{\sqrt{2\pi}\sigma} \exp\left[-\frac{(x_\tau - x_{\tau-1})^2}{2\sigma^2}\right]. \quad (6)$$

Here x denotes any single parameter of the full set of parameters n_i, T_i ; x_τ is the updated value and $x_{\tau-1}$ is the current value. At any given step, we update the value of a single parameter, keeping all the rest fixed, by generating a random number from the proposal distribution given above. The proposed point is retained in the chain with the probability

$$p = \min\left[1, \frac{P(s_{k,\tau}; \mathbf{n}_{\tau-1}, \mathbf{T}_{\tau-1} | \mathbf{D})}{P(s_{k,\tau-1}; \mathbf{n}_{\tau-1}, \mathbf{T}_{\tau-1} | \mathbf{D})}\right]. \quad (7)$$

In this expression we have chosen s_k as the parameter being updated and $\mathbf{n}_{\tau-1}$ and $\mathbf{T}_{\tau-1}$ are all the other parameters not equal to s_k ; P is the posterior PDF (eq. 5). A comma has been added in the subscript for greater clarity. If the point is accepted, then we replace $s_{k,\tau}$ with the nearest grid value in our template, since our template $\dot{\mathbf{C}}^{\text{th}}$ are calculated on a grid. The procedure is then repeated for all the other parameters sequentially to construct the chain.

Since our parameter space is compact, if the proposal point falls out of the box then we use periodic boundary condition to bring it back into the box. A moment's reflection shows that this does not affect the symmetry of the proposal density $q(x|x^*) = q(x^*|x)$, which is required to keep the condition for detailed balance. Although different σ s were chosen for the number density and temperature, their values were kept the same across the radial bins. Their values were chosen to ensure an acceptance rate of roughly 20–30 per cent, and typical σ values are larger than the grid size in n and T .

2.1.2 Central entropy profile

Any physical quantity that depends explicitly on thermodynamic variables can be estimated in a manner similar to the

one described above to estimate n_i, T_i by using the original chain in the parameter space to construct a subsidiary chain through

$$f_\tau = f(n_{i\tau}, T_{i\tau}), \quad (8)$$

where the function can depend on the full range of parameters or on only a few of them. As an example, the entropy in each radial bin can be estimated by constructing the following subsidiary chain (n_e is electron density simply related to the total number density once elemental abundance is known)

$$K_{i\tau} = T_{i\tau} n_{e,i\tau}^{-2/3}. \quad (9)$$

To isolate the behaviour of entropy near the centre of a cluster, we focus our attention on a few central annuli (for how these are chosen, see the first paragraph of section 2.1), say $i = 1, N_c$, where $N_c < N$. We then estimate the expectation values and covariance matrix for these entropies \bar{K}_i and $\text{cov}(i, j) \equiv \text{cov}(K_i, K_j)$. In principle we can now plot \bar{K}_i with error bars to display the range of entropy profiles allowed by the data. However, this is not optimal, and we find it useful to condense the large information available in the covariance matrix by fitting the entropy to an analytic profile. We find that the clusters analyzed by us display two kinds of behaviour: a) central cores and b) central cusps. Therefore, we choose the following models for the central entropy profile: (i) a flat core profile after [Cavagnolo et al. 2009](#)

$$K(R) = K_0 + K_{100} \left(\frac{R}{100 \text{ kpc}}\right)^\alpha; \quad (10)$$

(ii) a single power law profile

$$K(R) = K_1 \left(\frac{R}{100 \text{ kpc}}\right)^{\alpha_1}; \quad (11)$$

and (iii) a double power law profile

$$K(R) = K_1 \left(\frac{R}{100 \text{ kpc}}\right)^{\alpha_1} + K_2 \left(\frac{R}{100 \text{ kpc}}\right)^{\alpha_2}. \quad (12)$$

At this point we treat \bar{K}_i as the observed values of entropy. To fit the analytic expressions to these values, we construct the Fisher matrix from the inverse of the covariance matrix calculated above, $F_{ij} = \text{cov}(i, j)^{-1}$. The χ^2 for the proposed model is then given by

$$\chi^2 = \sum_i^{N_c} \sum_j^{N_c} (K(R_i) - \bar{K}_i) F_{ij} (K(R_j) - \bar{K}_j) \quad (13)$$

Using this and an expression equivalent to eq. 5, a Bayesian posterior PDF for the fit parameters (e.g., K_0 , K_{100} and α for the flat core profile) is obtained through a second MCMC analysis. Using the full covariance matrix takes into account the radial variation of entropy in individual chains, something that is not captured by using only the marginalised errors on the individual shell entropies.

2.2 Benchmarking the jMCMC method

We tested our jMCMC analysis on simulated as well as actual data. Simulated projected spectra were generated using XSPEC. We also used the *Chandra* observations of the cool-core cluster A2597 to further test the usefulness of our

method for actual data. The procedure used for generating the simulated data, and the Chandra observations of A2597 are described in the following sections.

2.2.1 Simulated Spectra

Simulated spectra for spherically symmetric shells of a cluster were generated using the *apec* model and the *fakeit* command in XSPEC. Profiles of intracluster gas density and temperature (shown with lines in Fig. 1) were generated assuming an NFW dark-matter potential (with concentration parameter $c_{200} = 3.3$, $M_{200} = 5.24 \times 10^{14} M_{\odot}$; Navarro et al. 1996) and a flat-core entropy profile (eq. 10; $K_0 = 37.9$ keV cm 2 ; $K_{100} = 117.9$ keV cm 2 and $\alpha = 1.11$). These density and temperature profiles were then used as inputs for simulating spectra from spherical shells, assuming a constant value of density and temperature in each shell. The elemental abundance was frozen to a constant value of one-third solar for all the shells, and a redshift (z) value of 0.05 was assumed for the cluster. The instrumental response files (Redistribution Matrix Files and Ancillary Response Files) required by the *fakeit* command were produced using the CIAO task *specextract* for an actual *Chandra* observation with *weight=no*. Spectra were simulated for an exposure time of 100 ks. The gas number density, $n(R)$, was used for obtaining the normalization of the APEC model (η), and the two are related through

$$\eta = \frac{10^{-14} \int n_e n_p dV}{4\pi D_A^2 (1+z)^2}, \quad (14)$$

where D_A is the angular diameter distance, n_e and n_p are the electron and proton number densities, and for one-third solar abundance $n_e = 0.53n$ and $n_p = n_e/1.2$. Assuming a constant gas density in each shell, the integral in the above equation reduces to $n_e^2 V/1.2$; where V is the volume of the shell.

As the observed emission from an astronomical object is always seen in projection along the line of sight, we produced projected spectra for all the annuli. For the i^{th} shell the projected spectrum was obtained by combining the simulated spectra from all the outer $k \geq i$ shells, weighted according to their projected volumes intercepted by the i^{th} shell (eq. 3). The projected spectra were combined in radial bins in order to contain a minimum of 10000 counts in each annulus. For each spectrum, channels were combined together in spectral bins so that each bin contains a minimum of 25 counts, so that the assumption of a χ^2 -distribution with Gaussian errors is valid. We also added a background to all spectral bins ($= 20\%$ of the source spectra with Poisson fluctuations) to the individual annuli spectra. The backgrounds (without the fluctuations) were then subtracted from the annuli spectra and the errors associated with background subtraction were propagated in the jMCMC analysis.

2.2.2 Test Cluster

We tested our jMCMC method for actual X-ray data using *Chandra* observations of the test cluster A2597. The rationale behind selecting A2597 as the test cluster is that it is a bright cool-core cluster with a deep (60.9 ks) *Chandra* observation. A log of the *Chandra* Observation of A2597 is

Table 1. Cluster sample.

Cluster Name	z	$\alpha(\text{J2000}), \delta(\text{J2000})$	Obsn. ID	Exp. Time (ks)
A85	0.0557	00 41 37.8, -09 20 33	15173	43.08
A133	0.0603	01 02 39.0, -21 57 15	2203	35.91
A478	0.0881	04 13 20.7, +10 28 35	1669	42.94
A1650	0.0823	12 58 36.76, -01 43 34.2	5823	40.13
A1795	0.0625	13 49 00.5, +26 35 07	493	19.88
A2029	0.0775	15 10 58.7, +05 45 42	4977	78.91
A2142	0.0899	15 58 20.00, +27 14 00.3	15186	91.07
A2204	0.151	16 32 45.7, +05 34 43	7940	78.16
A2244	0.0996	17 02 34.01, +34 04 41.1	4179	57.72
A2597 [†]	0.0824	23 25 19.70, -12 07 27.7	7329	60.90
A3112	0.0759	03 17 52.4, -44 14 35	13135	42.80
Hydra-A	0.0549	09 18 05.65, -12 05 44	576	19.52
A754	0.0535	09 08 50.1, -09 38 12	577	44.77
A2256	0.0581	17 03 43.5, +78 43 03	16129	44.49
A3158	0.0583	03 42 39.6, -53 37 50	3712	31.35
A3667	0.0552	20 12 33.68, -56 50 26.3	5751	130.60
ZWCL1215	0.0767	12 17 40.6, +03 39 45	4184	12.22

[†] Test cluster

given in Table 1. We also performed various tests on A2597 to optimize the jMCMC algorithm, which are discussed in Appendix A.

The data for this observation were obtained from the High Energy Astrophysics Science Archive Research centre (HEASARC). The CIAO version 4.7 and CALDB version 4.6.7 were used for analyzing the data. The data were reprocessed using the standard *chandra_repro* tool to produce the level 2 reduced event files (evt2) from the level 1 event files (evt1). Background event files matching with the source observation were produced using Maxim Markevitch's blank-sky background database¹. The source observation was cleaned of any flare contamination using the *lc_clean* script so as to match the blanksky background maps. Point sources were removed based on a visual inspection of the images. Spectra, background spectra and corresponding response files were generated for a number of circular annuli centred on the cluster's X-ray peak using the CIAO task *specextract*. The width of the annuli was chosen such that each annulus had at least 10000 counts in the 0.7-7.0 keV energy range².

Background Handling: The background in the blanksky and source observations is different due to both spatial and temporal variations of its different components. The major component of the background is due to the events produced by charged particles that dominates the >2keV energy range. The difference in the blanksky and source background due to the temporal variation of this component was corrected for by scaling the blanksky observations by the ratio of the source and blanksky count rates in the 9.5-12.0 keV energy range, where the Chandra effective area is close to zero. Another important background component is the Galactic diffuse soft X-ray background (SXB) that dominates below 1 keV. We checked for the SXB fluxes for

¹ see, <http://cxc.cfa.harvard.edu/contrib/maxim/acisbg>

² For some of the clusters analyzed in this paper, this condition was slightly relaxed in order to have at least one annulus within $R \leq 10$ kpc while for some of the bright clusters the condition was more constrained and the minimum counts were increased in order to have not more than 25 annuli in the cluster.

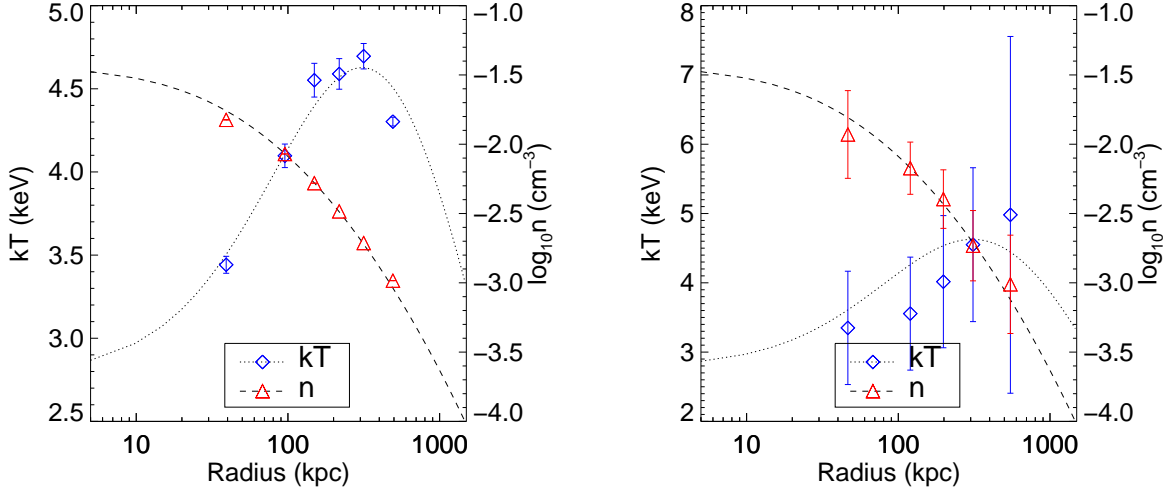


Figure 1. Density (red triangles) and temperature (blue diamonds) profiles obtained from the jMCMC analysis of the 100 ks (left) and 20 ks (right) simulated cluster spectra described in section 2.2.1. For comparison the input density and temperature profiles used for generating the simulated spectra are also shown.

all our clusters using ROSAT R45 (0.47-1.21 keV energy band) count rates just outside the clusters. In the faintest outermost annuli of two of our clusters (A2204 and A1650) the R45 SXB fluxes were found to be a significant fraction ($>15\%$) of the total 0.47-1.21 keV fluxes. For these clusters, SXB was modeled using the procedure described in [Vikhlinin et al. \(2005\)](#). For this, we extracted source and blanksky spectra from an off-axis region. The blanksky spectra were rescaled to match particle background in the source spectra. The residual (source minus rescaled blanksky) spectra from the off-axis regions were modeled using unabsorbed solar abundance mekal models. Then for both the clusters, the mekal models were subtracted from the individual annuli spectra (after properly scaling the mekal normalizations for the annuli areas). The spectral channels for all annuli spectra were combined in bins to have minimum 25 counts in each bin.

2.2.3 Cluster Sample

We carried out the jMCMC analysis on the *Chandra* X-ray observations of a sample of clusters selected from the statistically complete low-redshift sample of [Santos et al. \(2010\)](#). Our sample includes 17 clusters and spans a redshift range of 0.0535 to 0.151. The sample and the details of the observations used, are given in Table 1. The X-ray data was analyzed as described in the previous section, and the results are discussed in section 3. Results for some of the clusters from the low- z sample of [Santos et al. \(2010\)](#) are not shown in this paper mostly due to poor count statistics in their X-ray observations leading to too few annuli in the entropy profiles.

2.3 Results for simulated spectra and A2597

jMCMC analysis was carried out for the simulated and actual data as described in sections 2.1 & 2.2. Fig. 1 (left)

shows the density and temperature profiles obtained from the jMCMC analysis of the 100 ks simulated spectra. For comparison the actual input profiles are also shown. The jMCMC profiles are found to be consistent with the input profiles, and are unbiased. We also tested our method for simulated spectra produced using a lower exposure time of 20 ks. Due to fewer counts available, the minimum counts per spectrum for this analysis had to be reduced to 2500. The resulting temperature and density profiles and their comparison with the input profiles, are shown in Fig. 1 (right). Although the results are consistent with the input profiles, a lower exposure time leads to larger errors. This is expected as there are fewer counts per spectral bin. The density, temperature and entropy profiles obtained for the test cluster are shown in black color in Fig. 3.

2.4 Comparison with other methods

There are two recent analyses of radial entropy profiles which differ from each other: [Cavagnolo et al. \(2009\)](#) (henceforth, C09) and [Panagoulia et al. \(2014\)](#) (henceforth, P14). In C09, temperature profiles are directly obtained from the analysis of the 0.7-7.0 keV *projected* spectra. High resolution surface-brightness profiles and spectra in the 0.7-2.0 keV range are then used for obtaining high-resolution profiles of deprojected electron densities. The projected temperature profiles are interpolated to match the resolution of the density profiles. The density and temperature profiles are then combined to obtain the entropy profiles. The main advantage of C09's approach is that it gives an excellent resolution in the cluster core. The problem with their analysis is that the use of projected spectra leads to an overestimation of the temperature (and hence, entropy) in the central region.³ An earlier paper, [Donahue et al. \(2006\)](#), compared the entropy

³ We thank the anonymous referee for pointing out that the earlier Chandra observations also overestimated the

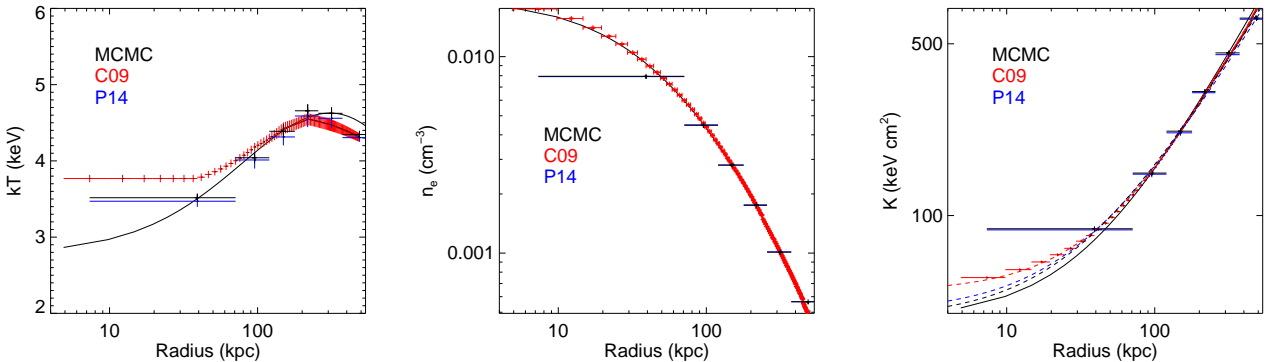


Figure 2. Temperature, electron number density and entropy profiles obtained using different analysis methods for the 100 ks simulated spectra. Results from jMCMC, C09’s and P14’s methods are shown using black, red and blue colors. The input electron density, temperature and entropy profiles used for generating the simulated spectra are also shown using black solid lines. The dashed black, red and blue lines in the third panel show the flat-core model (eq. 10) fits to the jMCMC, C09 and P14 entropy profiles, respectively.

profiles using projected and deprojected temperatures and found them to be similar (this is not quite correct; see left panels of Figs. 2 & 3). Panagoulia et al. (2014) deproject the spectra using the *DSDEPROJ* routine described in Russell, Sanders, & Fabian (2008). Profiles of electron density and temperature were obtained from the spectral analysis of the deprojected spectra, and were combined to obtain the entropy profiles.

The temperature, electron density and entropy profiles obtained using jMCMC, C09’s and P14’s analysis methods for the simulated spectra and the test cluster are shown in Figs. 2 and 3, respectively. C09’s method is found to overestimate the temperature in the inner annuli which is expected since the method makes use of projected spectra and hence inner annuli are contaminated by the hotter shells lying outside. Similarly, the temperature at larger radii is underestimated. Results from jMCMC analysis and P14’s method are found to be in good agreement with each other. For the test cluster, both these methods seem to overestimate the density in the outermost annulus. However, this is a common artifact of deprojection analyses due to the excess emission from shells outside the outermost annulus contributing to its emission.

2.5 Entropy profile with/without correlations

One downside of the standard deprojection methods is that they do not take into account the correlations between the deprojected parameters obtained for the different shells. To demonstrate this effect we fitted the entropy profile of the test cluster obtained from the jMCMC analysis using a flat-core model (eq. 10), as described in section 2.1.2. The expectation values of entropy for each shell \bar{K}_i and the entropy covariance matrix $\text{cov}(K_i, K_j)$ were calculated, which were then used in another MCMC analysis to obtain chains of K_0 , K_{100} and α . To see the effect of no correlation between the

entropies of different shells, we also carried out the same exercise with the non-diagonal terms of the entropy covariance matrix set to zero.

The K_0 - α and K_0 - K_{100} probability distributions and the resulting flat-core fits obtained from the two methods (with and without cross-covariance) are shown in the first two rows of Fig. 4. The expectation values of K_0 , K_{100} and α obtained using the full entropy covariance matrix are 11.31 ± 0.78 keV cm 2 , 101.47 ± 1.51 keV cm 2 and 1.37 ± 0.04 , respectively, and those obtained using only the diagonal terms are 11.84 ± 0.86 keV cm 2 , 99.71 ± 2.68 keV cm 2 and 1.42 ± 0.06 , respectively. Ignoring correlation between the entropies of different shells in the test cluster, therefore, does not seem to have any significant effect on the fitted parameters. The K_0 - α and K_0 - K_{100} probability distributions obtained from the two methods, however, do show some difference. For clusters with large covariances between the shell entropies, the effect of including correlations can be significant, as is seen for the cluster A3112, taken from the cluster sample analyzed in this paper. The K_0 , K_{100} and α values obtained for A3112, with and without considering correlation between shell entropies, are 2.04 ± 0.42 keV cm 2 , 135.14 ± 1.47 keV cm 2 and 0.95 ± 0.01 , and 2.35 ± 0.46 keV cm 2 , 129.17 ± 2.18 keV cm 2 and 0.94 ± 0.02 , respectively. The value of K_{100} for A3112, obtained from the two methods are, therefore, found to be significantly different. The K_0 - α and K_0 - K_{100} probability distributions for A3112 and the resulting flat-core fits obtained from the two methods (with and without cross-covariance) are shown in the last two rows of Fig. 4.

3 RESULTS FROM THE CLUSTER SAMPLE

The cluster sample described in section 2.2.3 was analyzed using the jMCMC method. The \mathbf{n}_e , \mathbf{T} chains resulting from the jMCMC analysis were combined to produce subsidiary entropy chains using $\mathbf{K} = \mathbf{T} \mathbf{n}_e^{-2/3}$. For each cluster, the elemental abundance in each annulus was fixed at the average value obtained from the analysis of the full (across all annuli) cluster spectrum. The resulting entropy profiles

temperature in 2-7 keV range; e.g., see section III A.1 in http://cxc.harvard.edu/caldb/downloads/Release_notes/CALDB_v4.html

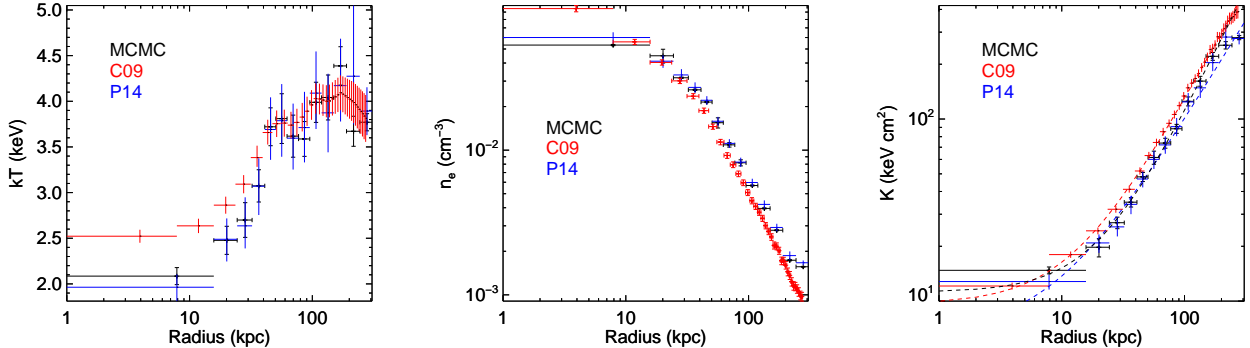


Figure 3. Temperature, electron number density and entropy profiles obtained using different analysis methods for the test cluster. Results from jMCMC analysis, C09’s method and P14’s method are shown using black, red and blue colors. The dashed black, red and blue lines in the third panel show the flat-core model (eq. 10) fits to the jMCMC, C09 and P14 entropy profiles, respectively.

Table 2. Flat-core entropy model (eq. 10) for the FC (flat-core) and PL (power law) samples. Here, $\text{DOF} = \text{number of annuli} - \text{number of fit parameters}$ (3 for a flat-core fit).

Cluster Name	K_0 (keV cm ²)	K_{100} (keV cm ²)	α	χ^2_{red} (DOF)
FC sample				
A133	13.4 ± 0.4	226.7 ± 10.8	1.76 ± 0.05	3.85 (5)
A1650	79.6 ± 10.0	108.7 ± 15.3	1.62 ± 0.25	0.53 (4)
A1795	28.7 ± 3.0	107.2 ± 17.3	2.03 ± 0.44	1.06 (11)
A2142	47.8 ± 11.8	150.3 ± 14.1	1.17 ± 0.17	0.57 (6)
A2204	7.8 ± 0.6	258.7 ± 15.8	1.98 ± 0.08	3.34 (4)
A2244	50.4 ± 13.4	116.8 ± 15.9	0.96 ± 0.16	1.067 (4)
A2597 [†]	11.2 ± 0.8	100.7 ± 1.6	1.40 ± 0.04	1.17 (8)
Hydra-A	11.5 ± 1.3	116.5 ± 2.3	1.25 ± 0.06	18.53 (6)
A754	263.0 ± 24.0	60.3 ± 25.8	1.82 ± 0.41	1.07 (10)
A2256	299.8 ± 21.0	17.8 ± 15.7	2.52 ± 1.02	8.36 (5)
A3158	229.7 ± 17.0	21.2 ± 17.9	4.32 ± 1.95	1.69 (3)
A3667	183.6 ± 16.2	61.1 ± 17.1	1.51 ± 0.28	3.71 (6)
ZWCL1215	305.7 ± 68.0	54.2 ± 32.7	1.90 ± 0.57	0.95 (5)
PL sample				
A85	3.4 ± 0.7	168.9 ± 2.2	1.00 ± 0.02	1.67 (8)
A478	3.5 ± 0.8	124.8 ± 2.4	1.03 ± 0.03	1.71 (13)
A2029	-1.7 ± 0.6	177.2 ± 1.8	0.81 ± 0.01	4.32 (12)
A3112	2.0 ± 0.4	135.1 ± 1.5	0.95 ± 0.01	12.74 (8)

[†]Test cluster

were then fitted using flat-core and power law models (eqs. 10–12), as described below.

3.1 Flat-Core model

The entropy profiles of the cluster sample were fitted with the flat-core model (eq. 10), using the entropy covariance matrices (see eq. 13) and the jMCMC method, as described in section 2.1.2. The resulting K_0 , K_{100} , α chains obtained for individual clusters plotted in the K_0 - α and K_0 - K_{100} planes along with their flat-core profile fits, are shown in Figs. 5–6. Almost all clusters of the sample show a positive correlation between K_0 and α , and an anti-correlation between K_0 and K_{100} . This (anti-)correlation is not sample correlation across clusters but only holds for individual clusters. The similarity of this correlation trend across clusters signifies the robustness of our technique and data quality, in-

dicating that the parameters of these clusters are well determined in comparison to those where the confidence regions show large scatter. Even in latter cases the general trends in correlation are present.

For the non-cool-core clusters with large errors in their entropy profiles (viz., A754, A3667, A3158, ZWCL1215 and A2256), the K_0 - α and K_0 - K_{100} probability distributions are found to be highly irregular and do not show any particular trend. The expectation values of K_0 , K_{100} and α (with the associated variances) and the reduced chi-squared values obtained for the individual clusters are given in Table 2. For a small subsample of the clusters (power law or PL sample comprising of A85, A2029, A478 and A3112; the remaining sample will be called flat-core or FC sample), the entropy flattening in the core was not that obvious (Table C2 shows that a flat-core fit is preferred over a single power-law even for the PL sample). The results of flat core entropy model fitting for the PL subsample are given in Fig. 6 and Table 2. The PL sample also shows a positive correlation between K_0 and α , and an anti-correlation between K_0 and K_{100} . The cluster A2029 is found to show an inverted entropy core; i.e., the entropy profile seems to steepen instead of flattening near the centre. The mean value of K_0 for this cluster is found to be negative and, therefore, is unphysical.

Since a flat-core profile (eq. 10) provides a better fit to entropy data of most of our clusters (F-test is shown in Table C2), we have moved the discussion of single and double power law fits to Appendix B & C, respectively.

4 DISCUSSION

As mentioned in the introduction, entropy, cooling time and $t_{\text{cool}}/t_{\text{ff}}$ profiles carry useful information about the physical processes in cluster cores. These profiles are sensitive to processes such as thermal conduction and multiphase condensation. In this section we discuss the implications of our results.

4.1 Comparison with previous works

The inverse method of peeling off spherically symmetric shells to obtain deprojected spectra does not take care of

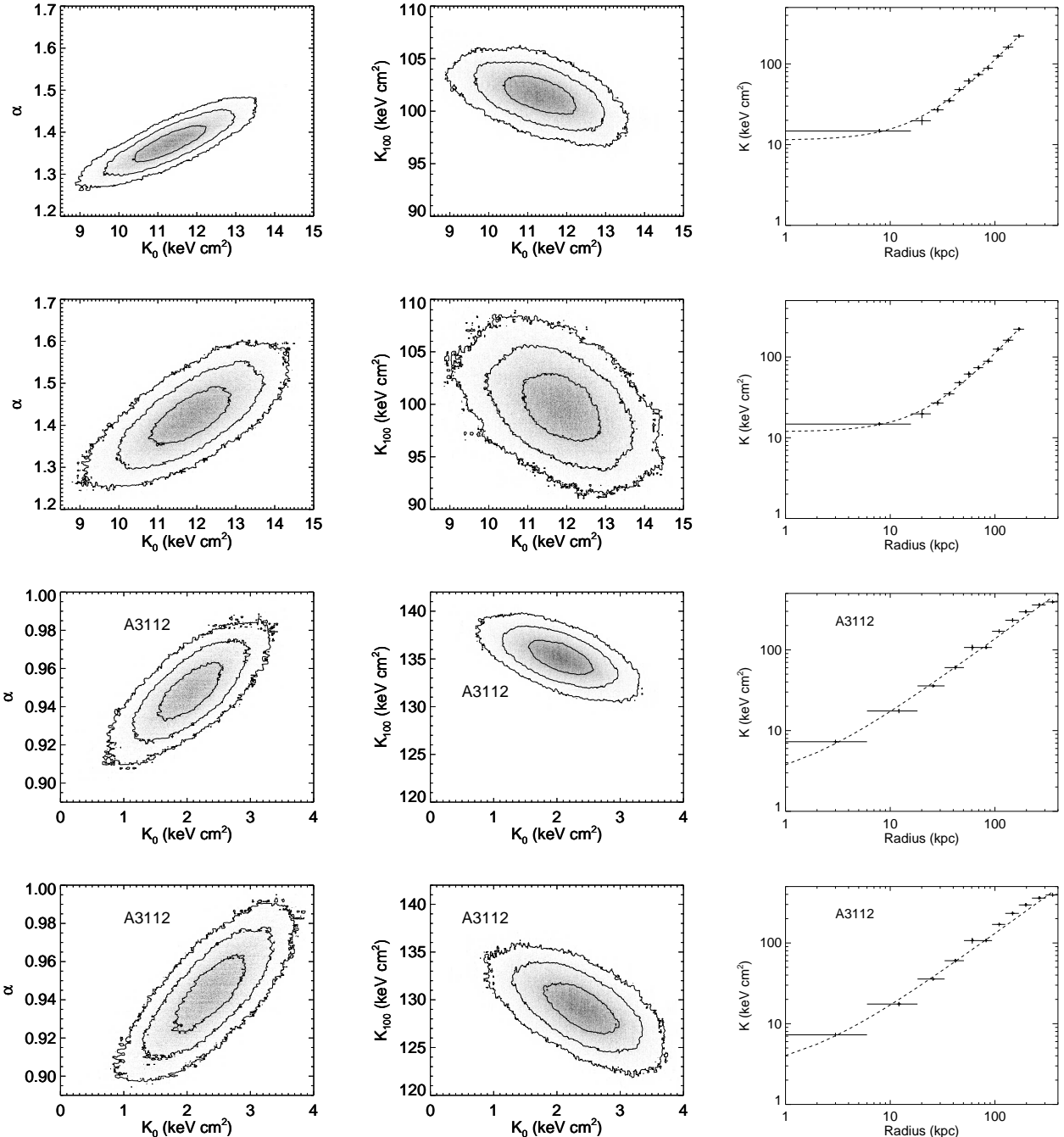


Figure 4. The 2D marginal probability distributions of $\alpha - K_0$ and $K_{100} - K_0$ obtained from the flat-core entropy profile fitting, with (first row) and without (second row) correlation between the shell entropies ($T_{\text{keV}}/n_e^{2/3}$) for the test cluster (A2597). Entropy profile of A3112 with and without correlation are also given in the third and fourth rows, respectively. The contours mark the 50%, 90% and 99% inclusion levels based on the density of points starting from the innermost contour outwards. Greyscale denotes the PDF density.

covariance of parameters corresponding to different shells. Using jMCMC method for data analysis enables clear visualization of the model parameter space. The method, however, has not been much used for analysing X-ray data of clusters. A joint Bayesian analysis of the *Chandra* and *ROSAT* data of the galaxy group NGC4325 was carried out by [Russell, Ponman, & Sanderson \(2007\)](#) using the MCMC method. The analysis was performed using a ‘forward fitting’ ap-

proach in which the gas density and temperature were assumed to have known parametrised functional forms. [Pizzolato et al. \(2003\)](#) also used parametric forms to deduce density/temperature profiles from the X-ray spectrum of A1795. While using parametrized models for density and temperature has several advantages, such as multiple datasets can be fitted together and the models can be extrapolated to large distances, its main disadvantage is that it introduces

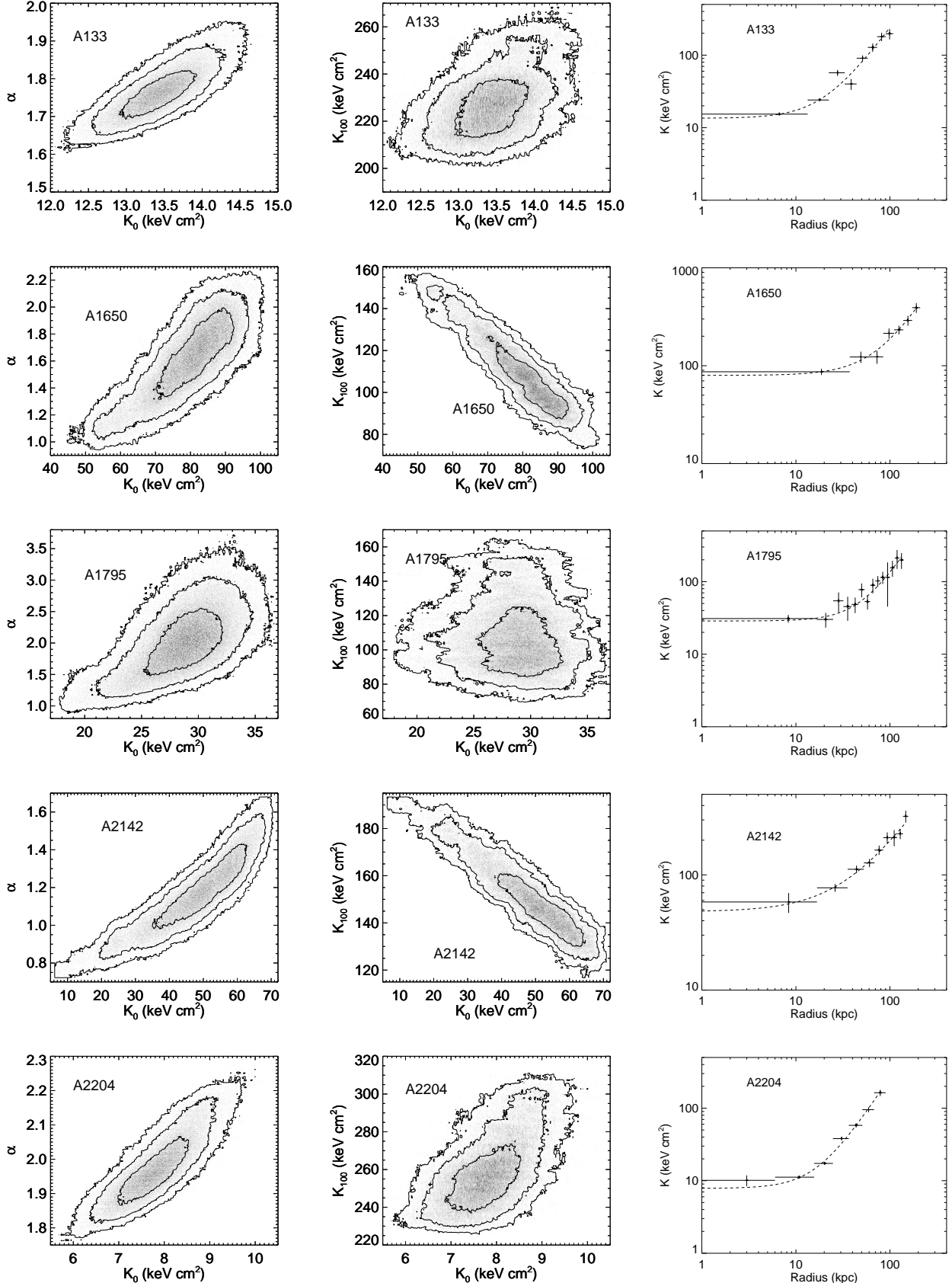


Figure 5. The K_0 - α and K_0 - K_{100} marginalized probability distributions obtained from the flat-core entropy model (eq. 10) fitting for FC (flat-core) sample. The contours mark the 50%, 90% and 99% inclusion levels based on the density of points starting from the innermost contour outwards. Greyscale denotes the PDF density.

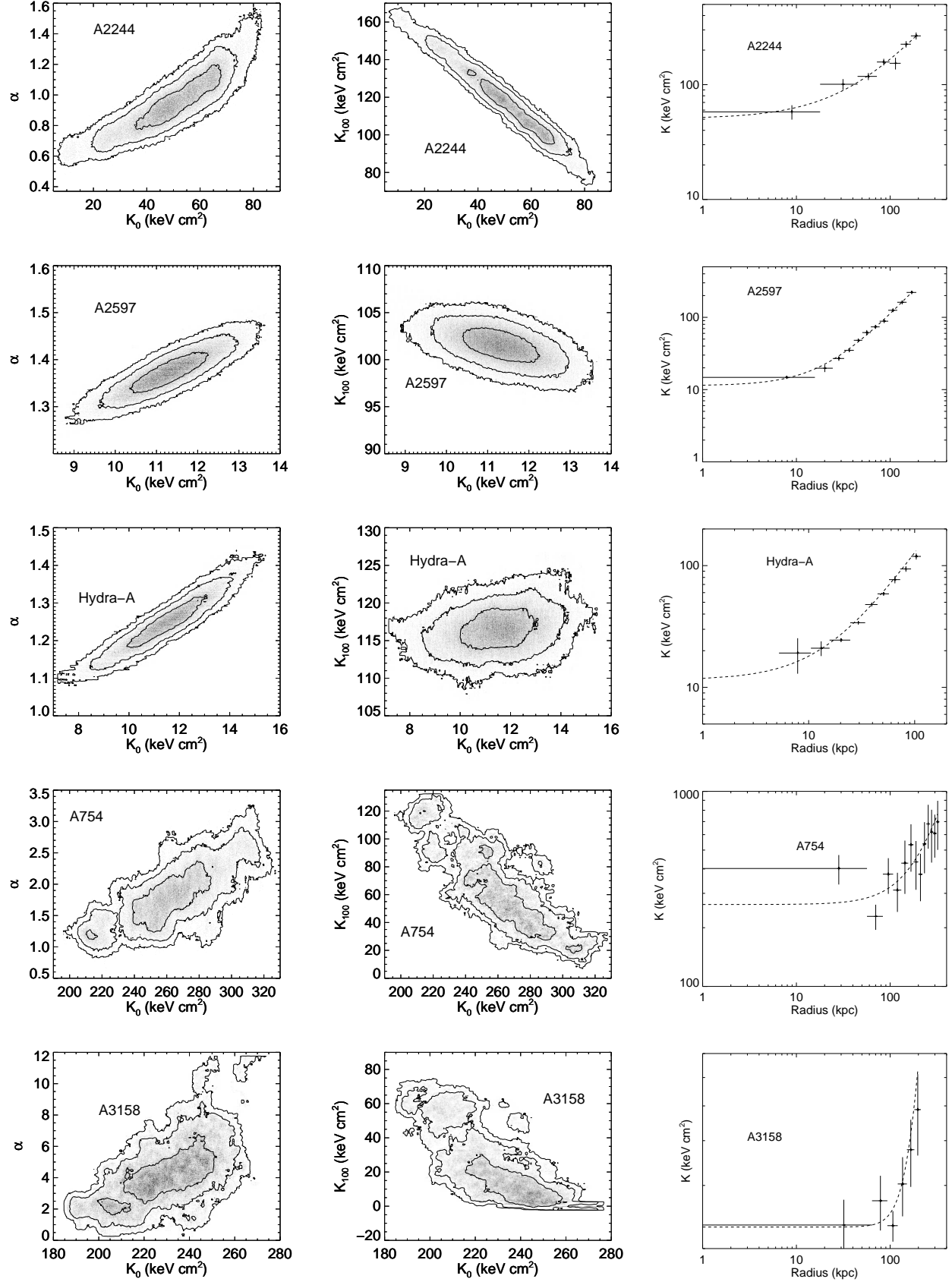


Figure 5. (Contd.)

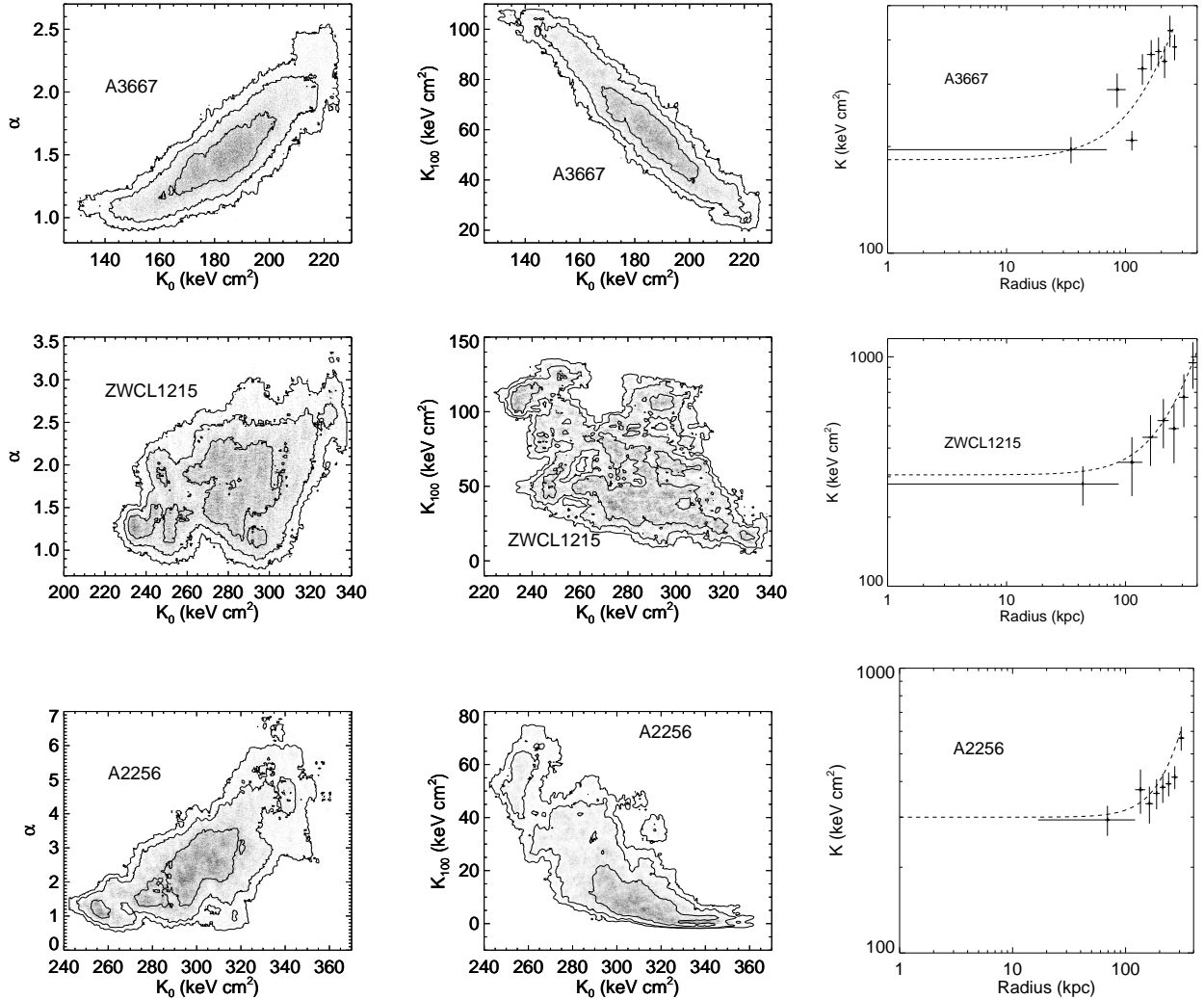


Figure 5. (Contd.)

inherent biases in the results. Our method can be improved for poor quality data by introducing regularization priors which impose smoothness on density and temperature profiles (e.g., Croston et al. 2006). Ameglio et al. (2007) applied MCMC maximum likelihood fitting to mock thermal Sunyaev-Zeldovich (tSZ) and X-ray surface-brightness maps from numerical simulations to deduce the de-projected density and temperature profiles (without using X-ray spectra). Even here, regularization was found to be essential to mitigate temperature oscillations.

We note that *DSDEPROJ* (an inverse method for spectral deprojection; Russell, Sanders, & Fabian 2008) may suffer from an intrinsic instability due to the following possibility: when the contribution from the outermost shell is subtracted from the next, any over/under estimate of photon counts—especially at high energies that best constrain the temperature—may cause an under/over estimate of photon counts deduced for the next shell. Since the correction appears with opposite signs in adjacent radial bins, albeit with diminishing volume factors, it may lead to an alternating over/under estimation of photon counts across the

radial bins that may show up as oscillating inferred temperature, even if the gas is not multiphase. This effect may be more pronounced for clusters with poor quality data with large Poisson noise. This problem may be avoided if we do not treat the data in annuli separately, but jointly across all radial bins. Russell, Sanders, & Fabian (2008) have argued that the oscillations mentioned above may also be caused by fitting a single-temperature model to a multiphase gas. It is straightforward to include multi-temperature plasma in our MCMC method, provided we have sufficiently high-quality data.

In a recent paper Sanders et al. (2014) have described a new MCMC based code *MBPROJ* that is in spirit very similar to our method. Unlike our method, which works only for those clusters that have high quality data since we use multiple spectral bins to fit the spectrum, by choosing only three spectral bins, *MBPROJ* can work even for clusters that have only a few thousand counts. It does that by assuming hydrostatic equilibrium; however, this assumption can be relaxed in the code to make it similar to our approach. To the best of our knowledge *MBPROJ* has not been used to

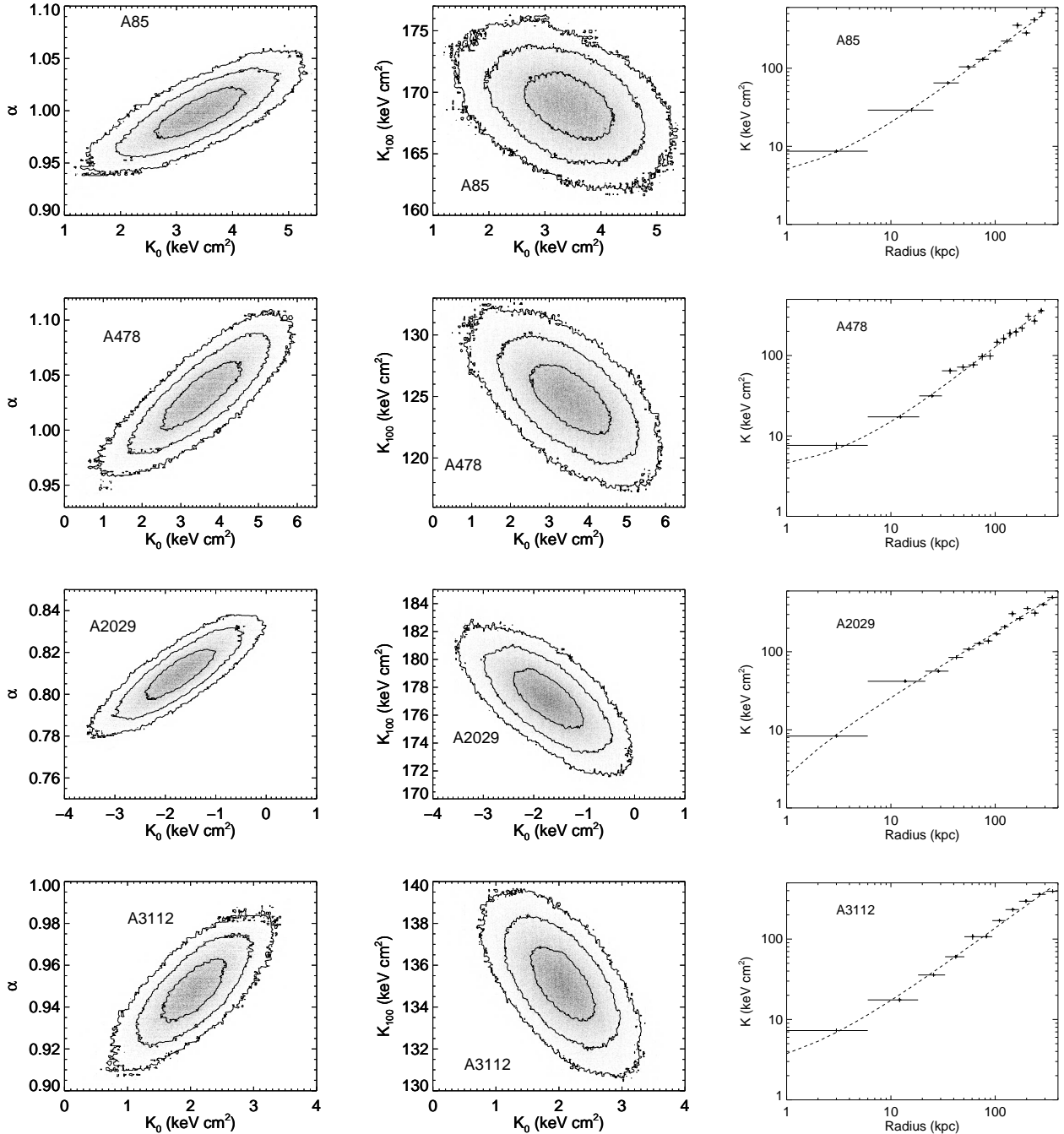


Figure 6. The K_0 - α and K_0 - K_{100} marginalized probability distributions obtained from the flat-core entropy model (eq. 10) fitting for the PL sample. The contours mark the 50%, 90% and 99% inclusion levels based on the density of points starting from the innermost contour outwards. Greyscale denotes PDF density.

analyze the entropy profiles of a cluster sample as we have done in this work.

4.2 Entropy core versus cusp

As discussed in section 2.4, our method agrees with the method adopted in P14 for simulated and the test cluster. Although our method does not agree with C09, the differences are well explained by the fact that not deprojecting

temperature leads to an increase in temperature inferred at the centre of clusters. Therefore, the method adopted in C09 is inherently biased to measure higher entropies in cluster cores, while P14 seems to be unbiased. However, the method of P14 does not account for the propagation of errors as the layers of a cluster are peeled off.

Given that the results from our analysis for the test cluster and simulated spectra agree with P14's method, in Fig. 7, in complete contrast, we find that most of the clusters an-

alyzed by us are actually better described by a cored power law model. Although, this is in overall agreement with C09, our tests show that our core entropy values are smaller than theirs for the coolest clusters (see top-left panel of Fig. 10). Note that all the non-cool core clusters (shown in red in Fig. 7; defined here as clusters with $K_0 > 100 \text{ keV cm}^2$) are consistent with flat cores. As expected, their central entropies are also higher. The blue curves corresponding to cool cores in Fig. 7, however, while mostly displaying flat cores, do have a sub-sample of about four clusters that are somewhat consistent with a single power law without any core (Fig. 6). However, their core entropy is so small ($K_0 \simeq 1 \text{ keV cm}^2$) that they could be well described as overall single power laws. Therefore, the question of core versus cusp depends somewhat on the scales that we are interested in.

Another discrepancy between P14 and C09 is the presence or absence of bimodality in the central values of entropy in clusters (see also Pratt et al. 2010). Although our sample of clusters is small, the second panel of Fig. 7 shows an apparent gap between the red and blue curves close to the centre of the clusters. This is indicated more clearly (with error bars) in the third panel. Most of the blue points are clustered at small K_0 , with smaller values of α (this is in contrast to Sanderson et al. 2014 who find a steeper entropy in cool cores). Then we see an apparent gap at about $K_0 \simeq 100 \text{ keV cm}^2$. The statistical significance of this gap is marginal due to small number of clusters in our sample, but seems to be in general agreement with the results of P14. Much further work is required to explore the issue of bimodality, and in the future we shall add more clusters to our sample to adequately address it.

While our results are broadly consistent with C09, our method is a significant improvement in terms of how we handle statistics. We are unable to fully explain our lack of agreement with P14, even though our tests show that our results match well on simulated data and a sample cluster, despite the difference in the two approaches. Most clusters in our sample have cores and not cusps; especially, the non-cool clusters display only cores. A few cool-core clusters are probably flat cored too, but with very small core radius, so our fits are only marginally able to capture the core.

P14's results are in complete disagreement with C09, and the former have argued that the difference is mainly due to the use of projected temperature profiles, large central radial bins (which might smooth out central gradients leading to flattening of entropy profiles) and assumption of single phase gas in the central regions by the latter. The first issue has been addressed in the present work as we have used deprojected temperature profiles in our analysis. In contrast to P14, in our analysis we found that using larger central radial bins for some of our clusters actually favours power law instead of flat-core profiles; an example of this is shown in Fig. 8.

There are some differences between our and P14's approach when it comes to fitting entropy profiles in the core. We, like C09, fit the parametric forms (power law, double power law, flat core) for *individual* clusters but P14 use a *common power law for all the clusters and groups in their sample* (see their Figs. 2 & 3). From the left panel of Fig. 7 we can see that a single power law indeed provides a good *common* fit for all the lowest entropy profiles. However, as we show in detail, individual cluster entropy profiles almost

always flatten towards the center. Another, and potentially more significant, difference is that our sample has clusters with temperature greater than 3 keV (see Table 1 in Santos et al. 2010) but P14's sample has several groups with temperature $\leq 1.2 \text{ keV}$ (see their Fig. 3). Their groups sample shows a good agreement with a single power law in the core compared to the full sample shown in their Fig. 2. The lowest entropy clusters (which are well fitted by a power law) in P14 may be dominated by small scale coronae associated with the massive central galaxy (e.g., see Sun 2009; see also Fig. 2 in Sharma et al. 2012b) rather than the typical large cool cores.

4.3 Cooling time & free-fall time

The cooling time and the gravitational free-fall time are important parameters that govern the properties of cluster cores (e.g., McCourt et al. 2012; Sharma et al. 2012a). Mittal et al. (2009) argue that the central cooling times better characterize the properties of cluster cores. Rafferty et al. (2008) find that the cooling time (t_{cool}) at 12 kpc (rather than the central cooling time or cooling time at the location of the central dominant galaxy) better delineates the star-forming versus non-star-forming clusters. This radius is close to the minimum of $t_{\text{cool}}/t_{\text{ff}}$ for most cool-core clusters. Since this radius is better resolved, and the cooling time at the very center is ambiguous, $\min(t_{\text{cool}}/t_{\text{ff}})$ is a good parameter to describe the cool cores. We therefore obtain the cooling time and $t_{\text{cool}}/t_{\text{ff}}$ profiles from our best-fit shell density and temperature values. While the cooling time is just a function of density, temperature and elemental abundance (the quantities obtained from X-ray observations) and is easy to obtain (middle panel of Fig. 9), the free-fall time requires the knowledge of gravitational acceleration profile. One way to obtain gravitational acceleration is by assuming hydrostatic equilibrium (e.g., see Rasia et al. 2006). While this is a good assumption for relaxed, cool-core clusters, non-cool clusters are generally merging clusters in which this assumption fails.

We obtain pressure profiles by combining density and temperature data. Since these pressure values are not always decreasing with radius (which is impossible for hydrostatic equilibrium), we fit an empirical form to obtain smooth pressure profiles

$$P(x) = \frac{P_0}{(x/a)^{\alpha_1} + (x/a)^{\alpha_2}}, \quad (15)$$

which is simpler compared to the ‘universal’ pressure profile suggested by Arnaud (2010). The left panel of Fig. 9 shows the pressure data and the best-fit pressure profiles for our cluster sample. Pressure (both data points and fits) decreases towards the centre for some non-cool clusters because of bulk flows and large turbulent velocities. Gravitational acceleration is obtained by differentiating pressure fits as

$$g_{\text{HSE}} \equiv -\frac{1}{\rho} \frac{dP}{dr},$$

where ρ is the gas mass density. Since pressure fits can have $dp/dr > 0$, g_{HSE} can be negative, resulting in an imaginary $t_{\text{ff}} \equiv (2r/g)^{1/2}$; we ignore such meaningless points in our analysis. Again, the red color corresponds to non-cool core

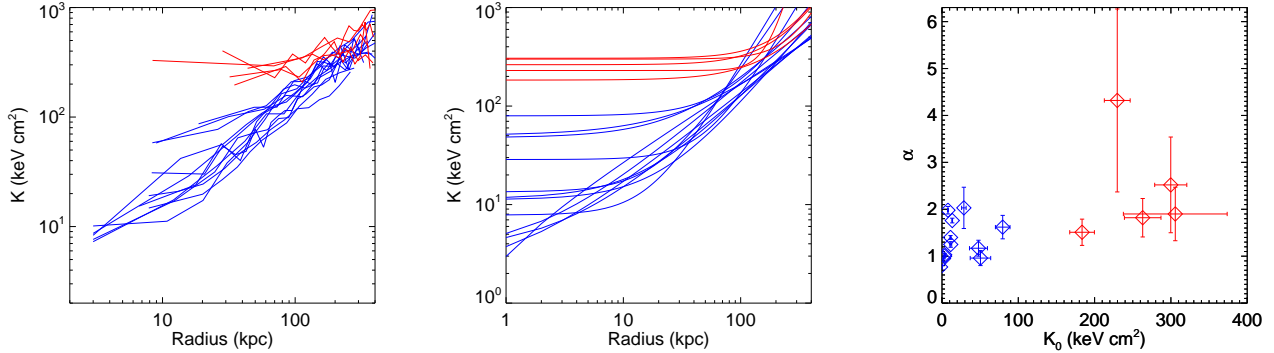


Figure 7. Entropy profiles of the full cluster sample obtained from the jMCMC fits (left) and the their flat-core profile fits (centre). The best-fit K_0 vs. α values obtained from flat-core fits is shown in the right panel. Cool-core ($K_0 < 100$ keV cm 2) and non-cool-core ($K_0 > 100$ keV cm 2) clusters are shown using blue and red colors, respectively.

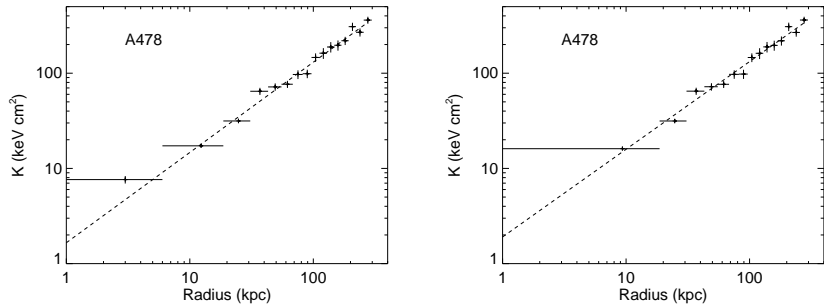


Figure 8. Entropy profiles of the cluster A478 with small (left) and large (right) central radial bins, fitted with single power law models (dotted lines). An excess entropy (flattening) is seen in the innermost annulus when a smaller radial bin size is used.

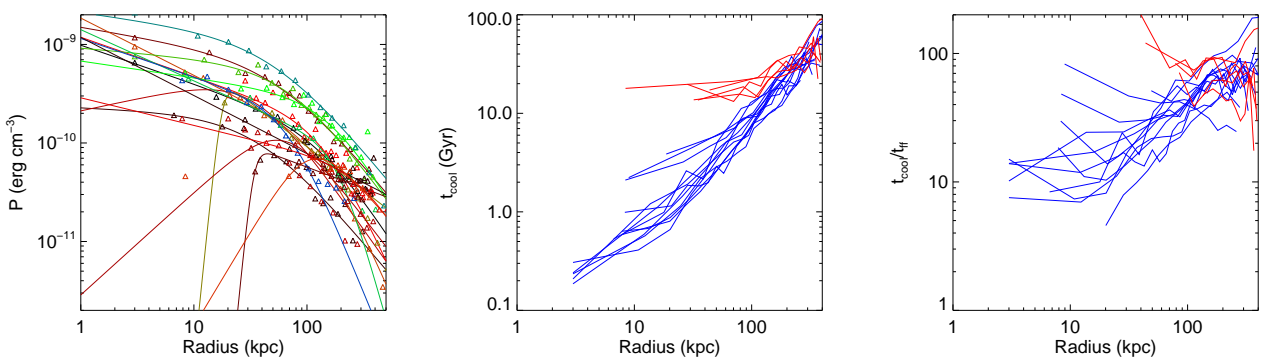


Figure 9. Left: The pressure profiles of the full cluster sample obtained from the jMCMC analysis (triangles) with the best-fit models (eq. 15) shown using lines. Different colors are used for different clusters. Middle and Right: The t_{cool} and $t_{\text{cool}}/t_{\text{ff}}$ profiles of the full cluster sample. Again, cool-core and non-cool-core clusters are shown using blue and red colors.

clusters, while blue is for cool-core clusters. Blue curves extend more towards smaller radii than the red ones because high/low central entropy/density means that non-cool clusters are not very bright at the centre and hence are difficult to resolve.

We show $t_{\text{cool}}/t_{\text{ff}}$ profiles for our cluster sample in the right panel of Fig. 9. From various recent studies (Wagh et al. 2014; Banerjee & Sharma 2014; Tremblay et al. 2015; Voit et al. 2015), it appears that this ratio plays a key role

in determining the amount of cold gas and AGN feedback in cluster cores. Cold gas condensation and signatures of AGN feedback (in form of radio emission and X-ray cavities) are expected if this ratio falls below a critical value close to 10 (Meece et al. 2015; Choudhury & Sharma 2015). Moreover, clusters are not expected to fall too much below this threshold as extreme feedback due to cold gas condensation is triggered in that case which pushes the gas out and main-

tains $\min(t_{\text{cool}}/t_{\text{ff}})$ close to the critical value. Indeed, in all our cases $t_{\text{cool}}/t_{\text{ff}} \gtrsim 4$.

The top-left panel of Fig. 10 shows the core entropy derived from C09 (ACCEPT sample) as a function of the same quantity derived from our jMCMC analysis. For core entropy (K_0) larger than 10 keV cm² the two methods agree with each other. However, for the lowest core entropies obtained from our jMCMC analysis the ACCEPT core entropies seem to flatten out (i.e., are significantly larger). We can speculate on the saturation of core entropy in C09's analysis. First, of course, C09 uses projected temperatures which overestimates the entropy in the core. However, this is not large enough to explain the observed discrepancy in the coolest cores. C09 fit the flat-core entropy profile (eq. 10) over *all* their radial shells but *we integrate the PDF over the outermost radial shells* and then obtain the marginalized densities and temperatures for the inner shells (extending up to $\lesssim 300$ kpc). Only after this, do we fit a flat-core entropy profile over these shells. The entropy values in the outermost shells for the discrepant coolest cores show a steepening of the entropy profile in the outermost shells. Thus, having to fit larger entropy value for the outermost shells may lead to an overestimate of the core entropy (K_0) in C09. More work is needed to fully understand this discrepancy.

Different panels of Fig. 10 show correlation of X-ray properties derived from our analysis and observations from other wavebands (obtained from ACCEPT⁴ tables; Cavagnolo et al. 2009), namely, $H\alpha$ and radio. We also compare our results with those of Voit & Donahue (2015). Like them, we find that the *amount* of $H\alpha$ luminosity is anti-correlated with $\min(t_{\text{cool}}/t_{\text{ff}})$, albeit with some scatter. A similar trend is seen for radio luminosity but the spread is larger. Anti-correlation is not as strong with the core entropy (K_0). The large scatter is consistent with the cyclic behaviour observed in cool core simulations (compare with Fig. 14 of Prasad et al. 2015; note that these are data from a single simulation and do not span as large a range in K_0 and $\min(t_{\text{cool}}/t_{\text{ff}})$ as seen in our Fig. 10). One aspect in which we differ from Voit & Donahue (2015) is that, unlike them, we do not see $H\alpha$ emitting systems with $\min(t_{\text{cool}}/t_{\text{ff}} \gtrsim 10)$; they have several $H\alpha$ emitting clusters with largest $\min(t_{\text{cool}}/t_{\text{ff}}) \gtrsim 20$. This discrepancy is closely related to the saturation of core entropy for coolest clusters in C09 (and hence under/over-estimation of core density/cooling time), discussed in the previous paragraph. Other factor that can systematically bias their $t_{\text{cool}} \propto T/\Lambda(T)$ high is the fact that they use *projected* temperatures which are larger than the actual temperatures (which our jMCMC method faithfully reproduces) in spherical shells (see left panels of Figs. 2 & 3). Another difference is the computation of t_{ff} which depends on how well the pressure fit approximates the pressure data (see left panel of Fig. 9). Voit et al. (2015) introduce a singular isothermal potential with $\sigma = 250$ km s⁻¹ at all their cluster centers; this can lead to a shorter t_{ff} and a higher $t_{\text{cool}}/t_{\text{ff}}$. One more minor difference from Voit et al. (2015) is that we have two clusters with $\min(t_{\text{cool}}/t_{\text{ff}}) < 10$ with no $H\alpha$ detection. Sorting out these disagreements is left for future.

5 CONCLUSIONS

Following are the key conclusions of our paper:

- jMCMC method is a statistically accurate method to recover the density and temperature profiles in cluster cores, which accounts for covariance between density and temperature of different shells.
- Most cluster cores favour a flat entropy core and not a power law (neither a single or a double power law), on the scales of 10 kpc. A single power law is clearly favoured in only one of the clusters in our sample. One must specify a scale when talking about flattening of the entropy profile as some clusters and groups show a decrease in entropy at scales \lesssim few kpc, corresponding to small coronae associated with BCGs.
- The entropy and cooling time distributions may indicate bimodality but more clusters are required to reach definitive conclusions.
- The minimum value of $t_{\text{cool}}/t_{\text{ff}}$ appear to govern the presence of $H\alpha$ and radio emission in cluster cores. The *amount* of cold gas is anti-correlated with $\min(t_{\text{cool}}/t_{\text{ff}})$, but with a large scatter.
- The core entropy for coolest cores is systematically overestimated by C09 as compared to our jMCMC method, resulting in a lower density, a longer cooling time, and a larger $\min(t_{\text{cool}}/t_{\text{ff}})$. The discrepancies in the observational reconstruction of thermodynamic profiles need to be sorted out before a detailed comparison with theoretical models can be made.

Acknowledgements: This work is partly supported by the DST-India grant no. Sr/S2/HEP-048/2012 (which also supports KL) and an India-Israel joint research grant (6-10/2014[IC]). We thank the anonymous referee for suggestions which substantially improved our paper.

REFERENCES

Allen S. W., Everard A. E., & Mantz A. B. 2011, ARAA, 49, 409
 Ameglio S., Borgani S., Pierpaoli E., & Dolag K. 2007, MNRAS, 382, 397
 Anders E., Grevesse N., 1989, GeCoA, 53, 197
 Anders E., Ebihara M., 1982, GeCoA, 46, 2363
 Anderson M. & Bregman J. N. 2010, ApJ, 714, 320
 Arnaud K. A., 1996, ASPC, 101, 17
 Banerjee N., Sharma P., 2014, MNRAS, 443, 687
 Arnaud M., Pratt G. W., Piffaretti R., Böhringer H., Croston J. H., & Pointecouteau E., 2010, A&A, 517, A92
 Cavagnolo K. W., Donahue M., Voit G. M., & Sun M. 2009, ApJS, 182, 12
 Choudhury P. P., Sharma P. 2016, MNRAS, 457, 2554
 Collies M., Dalton G., Maddox S. et al. 2001, MNRAS, 328, 1039
 Croston J. H., Arnaud M. A., Pointecouteau E., Pratt G. W., 2006, A&A, 459, 1007
 Croston J. H., Pratt G. W., Böhringer H. et al. 2008, A&A, 487, 431
 Davis M., Efstathiou G., Frenk C. S., & White S. D. M. 1985, ApJ, 292, 371
 Donahue M., Horner D. J., Cavagnolo K. W., Voit G. M., 2006, ApJ, 643, 730
 Eke V. R., Cole S., & Frenk C. S. 1996, MNRAS, 282, 263
 Gaspari M., Ruszkowski M., & Oh S. P., 2013, MNRAS, 432, 3401
 Hastings W. K., 1970, Biometrika, 57, 97

⁴ www.pa.msu.edu/astro/MC2/accept/

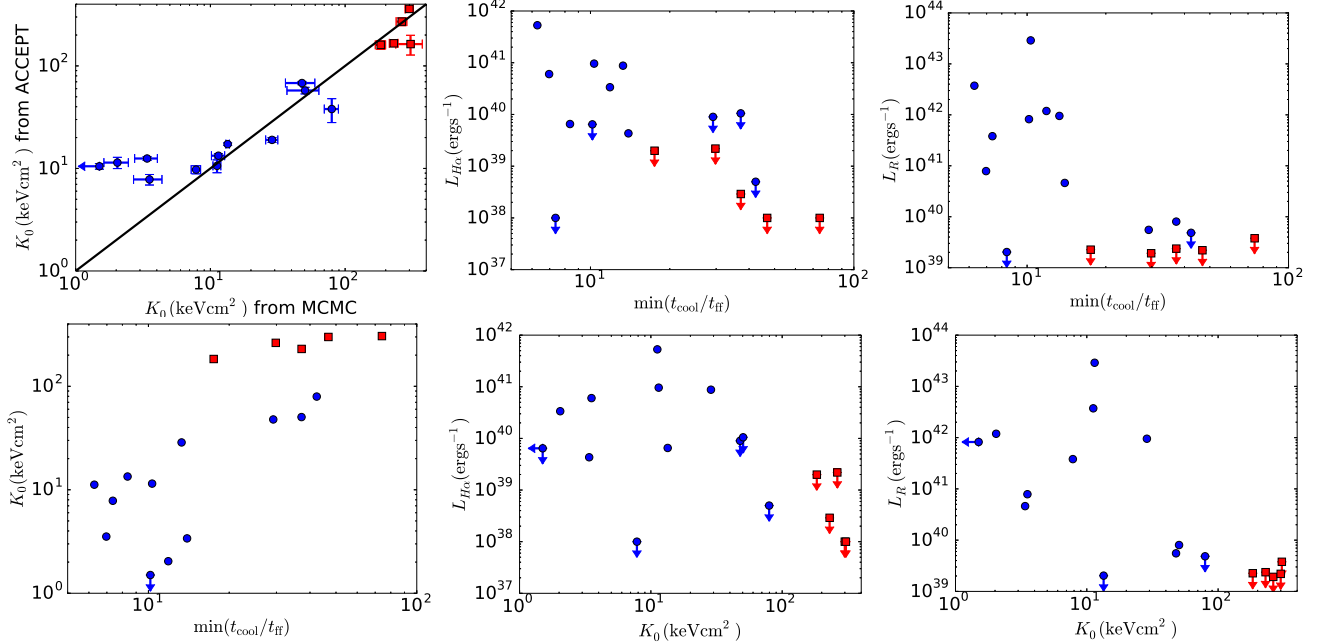


Figure 10. Correlation between various important quantities derived from our analysis (K_0 and $\min(t_{\text{cool}}/t_{\text{ff}})$ are derived from jMCMC; see middle panel of Fig. 7 and the right panel of Fig. 9) and from the ACCEPT sample (where radio and $H\alpha$ luminosities are listed). Although our sample is a small subset of their, our trends are generally similar to Voit & Donahue (2015). Top-left panel shows that the core entropy values for our coolest cores are systematically smaller than those in the ACCEPT sample (solid black line is the 1:1 line). We have a smaller fraction of non-cool cores compared to C09.

Hudson D. S., Mittal R., Reiprich T. H. et al. 2010, A&A, 513, A37

Kaiser N., 1991, ApJ, 383, 104

Kriss G. A., Cioffi D. F., Canizares C. R., 1983, ApJ, 272, 439

McCourt M., Sharma P., Quataert E., Parrish I. J. 2012, MNRAS, 419, 3319

McNamara B. R., Nulsen P. E. J. 2007, ARAA, 45, 117

Meece G. R., O'Shea B. W., & Voit, G. M., 2015, ApJ, 808, 43

Metropolis, N., Rosenbluth, A. W., Rosenbluth, M. N., Teller, A. H., & Teller, E. 1953, The Journal of Chemical Physics, 21, 1087

Morrison R., McCammon D., 1983, ApJ, 270, 119

Mittal R., Hudson D. S., Reiprich T. H., & Clarke T. 2009, A&A, 501, 835

Navarro J. F., Frenk C. S., & White S. D. M., 1996, 462, 563

Panagoulia E. K., Fabian A. C., & Sanders J. S. 2014, MNRAS, 438, 2341

Pizzolato F., Molendi S., Ghizzardi S., De Grandi S. 2003, ApJ, 592, 62

Pizzolato F. & Soker N., 2005, ApJ, 632, 821

Prasad D., Sharma P., & Babul A. 2015, ApJ, 811, 108

Pratt G. W., Arnaud M., Piffaretti R. et al. 2010, A&A, 511, A85

William H. Press, Saul A. Teukolsky, William T. Vetterling, and Brian P. Flannery. 2007. Numerical Recipes 3rd Edition: The Art of Scientific Computing (3 ed.). Cambridge University Press, New York, NY, USA

Putman M. E., Peek J. E. G., & Joung, M. R. 2012, ARAA, 2012, 50, 491

Rafferty D. A., McNamara B. R., Nulsen P. J. R., 2008, ApJ, 687, 899

Rasia E., Ettori S., Moscardini L., Mazzotta P., Brogan S., Dolag K., Tormen G., Cheng L. M., & Diaferio A., 2006, MNRAS, 369, 2013

Rossetti M. & Molendi S. 2010, A&A, 520, A83

Russell P. A., Ponman T. J., Sanderson A. J. R., 2007, MNRAS, 378, 1217

Russell H. R., Sanders J. S., Fabian A. C., 2008, MNRAS, 390, 1207

Sanders J. S., Fabian A. C., Hlavacek-Larrondo J., Russell H. R., Taylor G. B., Hofmann F., Tremblay G., Walker S. A., 2014, MNRAS, 444, 1497

Sanderson J. R., O'Sullivan E., & Ponman T. J., 2009, MNRAS, 395, 764

Santos J. S., Rosati P., Tozzi P., et al. 2008, A&A, 483, 35

Santos J. S., Tozzi P., Rosati P., Böhringer H., 2010, A&A, 521, A64

Sharma P., McCourt M., Quataert E., Parrish I. J. 2012, MNRAS, 420, 3174

Sharma P., McCourt M., Parrish I. J., & Quataert, E. 2012, MNRAS, 427, 1219

Smith R. K., Brickhouse N. S., Liedahl D. A., Raymond J. C., 2001, ApJ, 556, L91

Sun M., 20009, ApJ, 704, 1586

Tozzi P. & Norman C. 2001, ApJ, 546, 63

Tremblay G., O'Dea C. P., Baum S., et al., 2015, MNRAS, 451, 3768

Vikhlinin A., Markevitch M., Murray S. S., Jones C., Forman W., Van Speybroeck L., 2005, ApJ, 628, 655

Voit G. M., Balogh M. L., Bower R. G., Lacey C. G., Bryan G. L., 2005, MNRAS, 364, 909

Voit G. M., Donahue M., 2015, ApJL, 799, L1

Voit G. M., Donahue M., Bryan G. L., & McDonald M., 2015, Nature, 519, 203

Wagh B., Sharma P., & McCourt M., 2014, MNRAS, 439, 2822

White S. D. M. & Rees M. J. 1978, 183, 341

APPENDIX A: OPTIMIZING JMCMC

We performed various tests on A2597 to optimize the jMCMC algorithm. Based on the results of these tests we made

certain choices that apply to the rest of the cluster sample analyzed in the paper. For most of our analyses the elemental abundance, Z , in all the annuli spectra was assumed to be equal to the average elemental abundance of the cluster obtained from the analysis of the cluster's full spectrum in XSPEC. To check for the effect of a variable Z , we added Z_i as an additional parameter for the i^{th} shell along with n_i and T_i . To keep the size of model spectra (\mathbf{M}_{iJ}) manageable we reduced the number of n and T grid points to half for this test (i.e., from 500 and 150 to 250 and 75; see section 2.1.1). The Z parameter was added as a third-axis to this box with 5 linearly distributed values between 0.2 to 1.0 times the solar elemental abundance value.

Having too many annuli in our analysis makes it computationally slow, and can lead to large errors in the parameters. On the other hand, having few annuli can lead to the inner regions of the cluster not being resolved properly. Therefore, we tested for the effect of varying the number of annuli used for the analysis. Minimum ~ 17000 counts in each annulus led to 13 annuli in A2597. The minimum counts were increased to ~ 30000 and decreased to ~ 12000 to have a total of 6 and 18 annuli, respectively. We carried out the jMCMC analysis of A2597 with 6, 13 and 18 annuli. We also investigated the effect of changing the length of MCMC chains. The results from all these tests are discussed below.

- *Fixed vs. variable elemental abundance:* The electron number density, temperature and entropy profiles obtained from the jMCMC analysis of the test cluster A2597 are shown in Fig. A11. The profiles obtained with a variable elemental abundance are also shown. The figure shows that a free elemental abundance does not affect the density and entropy profiles significantly. As we are mostly interested in the entropy profiles of the clusters, we have *fixed the elemental abundance* for the analysis of the remaining clusters at their respective average values obtained from spectrum integrated over all shells. This is essentially done for computational reasons.

- *The number of annuli:* The test cluster was analyzed with different number of annuli and the resulting entropy profiles are shown in Fig. A12. It can be seen that varying the number of annuli does not change the general shape of the entropy profile, especially at resolved radii. However, note that with just 6 annuli one can not constrain the profile shape very well. For example, the flattening of the entropy profile towards the centre seen with 13 and 18 annuli, does not seem to be very prominent in the profile with just 6 annuli. On the other hand, having 18 annuli leads to large errors in the inner entropy values and therefore can lead to a poor fit. In general, for the rest of the sample, we try to optimise in terms of best resolution of the cluster core profiles.

- *Number of steps:* We tried different numbers of steps (2000, 5000, 10000 and 20000) in the MCMC random walk along *each* parameter direction for the test cluster, and the temperature, electron density and entropy profiles obtained are shown in Fig. A13. The profiles are found to be mostly consistent with each other. However, it can be seen that using 2000 steps gives slightly larger error bars, especially in the temperature profile, and the mean values also seem to be

Table B1. Single power law entropy model fitting (eq. 11) for PL sample.

Cluster Name	K_1 (keV cm 2)	α_1	χ^2_{red} (DOF)
A85	173.3 \pm 2.1	0.92 \pm 0.01	4.09 (9)
A478	130.5 \pm 1.9	0.95 \pm 0.01	2.65 (14)
A2029	173.3 \pm 1.2	0.84 \pm 0.01	4.75 (13)
A3112	144.6 \pm 0.9	1.44 \pm 0.01	18.24 (9)

Table C1. Double power law entropy model fitting (eq. 12).

Cluster Name	K_1 (keV cm 2)	α_1	K_2 (keV cm 2)	α_2	χ^2_{red} (DOF)
A85	41.5 \pm 29.7	0.49 \pm 0.20	129.2 \pm 30.5	1.12 \pm 0.10	6.37 (7)
A133	17.7 \pm 3.1	0.09 \pm 0.06	227.7 \pm 10.3	1.86 \pm 0.09	5.21 (4)
A478	11.9 \pm 8.0	0.29 \pm 0.18	116.0 \pm 8.7	1.07 \pm 0.05	2.40 (12)
A1650	130.6 \pm 28.4	0.26 \pm 0.13	58.7 \pm 27.6	2.34 \pm 0.81	1.35 (3)
A1795	53.4 \pm 17.2	0.26 \pm 0.15	80.6 \pm 23.9	2.26 \pm 0.57	0.59 (10)
A2029	0.4 \pm 0.3	0.33 \pm 0.72	169.9 \pm 12.4	0.87 \pm 0.13	8.89 (11)
A2142	120.9 \pm 37.8	0.39 \pm 0.16	75.2 \pm 39.2	1.94 \pm 0.94	1.44 (5)
A2204	10.3 \pm 2.5	0.09 \pm 0.08	261.3 \pm 14.1	2.03 \pm 0.09	5.24 (3)
A2244s	139.7 \pm 18.9	0.38 \pm 0.10	25.6 \pm 18.5	2.32 \pm 1.08	2.06 (3)
A2597	16.1 \pm 4.2	0.12 \pm 0.08	95.3 \pm 4.8	1.46 \pm 0.07	1.65 (7)
A3112	5.2 \pm 4.8	0.18 \pm 0.15	131.9 \pm 5.1	0.96 \pm 0.02	18.24 (7)
Hydra-A	16.2 \pm 4.6	0.11 \pm 0.09	102.8 \pm 4.8	1.30 \pm 0.07	3.94 (5)
A754	293.2 \pm 29.9	0.23 \pm 0.15	39.0 \pm 22.4	1.78 \pm 0.52	1.31 (9)
A2256	298.2 \pm 22.4	0.15 \pm 0.11	12.0 \pm 12.8	2.47 \pm 1.06	4.63 (4)
A3158	261.6 \pm 33.8	0.22 \pm 0.17	0.3 \pm 25.6	3.23 \pm 2.00	5.36 (2)
A3667	211.9 \pm 18.6	0.15 \pm 0.10	35.6 \pm 16.6	1.83 \pm 0.47	4.97 (5)
ZWCL1215	305.9 \pm 38.0	0.32 \pm 0.18	39.1 \pm 25.1	1.68 \pm 0.61	0.41 (4)

slightly shifted from the rest of the profiles. Profiles for larger number of steps are found to be almost identical. Although for the test cluster 5000 steps seems to be an optimum value at which the results seem to be converging, considering that many of our clusters have poor count statistics, we chose 100000 steps as a safe value for our analysis.

APPENDIX B: SINGLE POWER LAW MODEL

Since the entropy profiles of PL sample showed almost linear shapes in the log-log plot, single power law model (eq. 11) fits were tested for these clusters. The resulting K_1 - α_1 probability distributions, along with the single power law profile fits are shown in Fig. B14. All the clusters of PL sample show a weak positive correlation between K_1 and α_1 , except for A2029, which does not show any correlation between them. The expectation values of K_1 and α_1 (with the associated variances) and the reduced chi-squared values obtained from the fits are given in Table B1. The flat-core and single power law model fits for PL sample were compared using F-test and the results are given in Table C2. Flat-core fits seem to be preferred compared to single power law fits for all the clusters of PL sample (this is of course true for the FC sample). However, since for the cluster A2029, flat-core model fitting leads to negative K_0 , single power law fit may be a preferred.

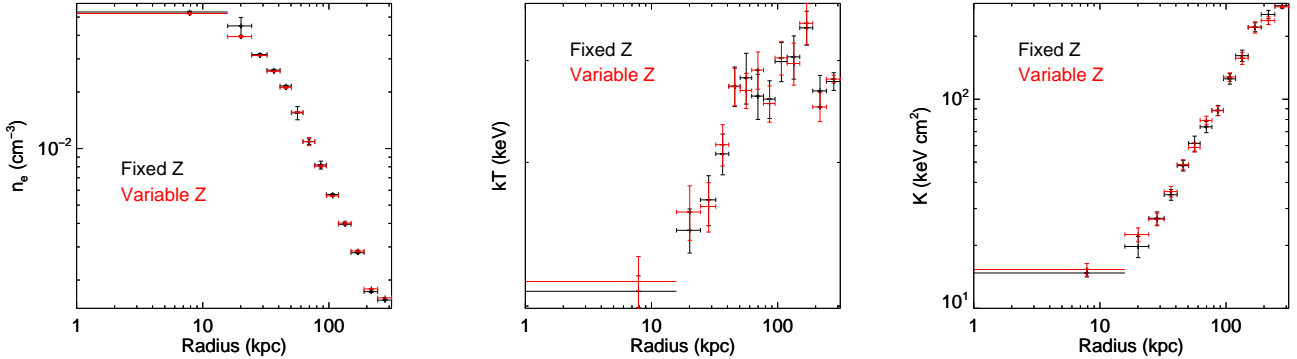


Figure A11. Electron density, temperature and entropy profiles obtained from the jMCMC analysis of the Chandra observations of the test cluster A2597. Profiles obtained with fixed and variable elemental abundance are shown using black and red colors, respectively.

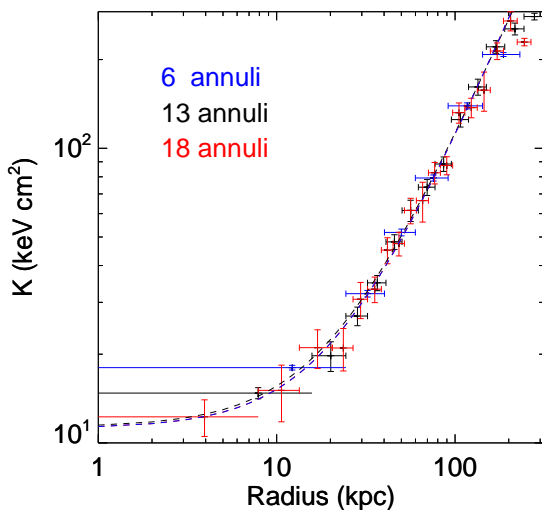


Figure A12. Entropy profiles obtained from the jMCMC analysis of the test cluster using 6 (blue), 13 (black) and 18 (red) annuli. The flat-core model fits are also shown using dashed lines.

APPENDIX C: DOUBLE POWER LAW MODEL

One of the main results of P14 has been that the entropy profiles of all clusters in their sample were found to be best-fitted using single/double power law models. Therefore, we have also tried double power law (eq. 12) fits for our full cluster sample⁵. To avoid any degeneracy between the two power laws, we have forced the conditions $\alpha_1 < \alpha_2$ and $\alpha_1, \alpha_2 > 0$, so that the first power law fits the central region (where almost all the clusters show flattening) and the second power law fits the outer parts of the clusters. The resulting $K_1-\alpha_1$ and $K_2-\alpha_2$ probability distributions, along with the double power law profile fits are shown in Fig. C15. Nearly all the clusters of the sample show a positive correlation between K_1 and α_1 , and a negative correlation between

K_2 and α_2 . The cluster, A2029, which showed an inverted core in the flat-core fit, shows a poor fit with the double power law model; the $K_1-\alpha_1$ probability distribution for this cluster seems to be highly irregular although the $K_2-\alpha_2$ plot looks symmetric with no visible correlation between the two quantities. The expectation values of K_1 , α_1 , K_2 and α_2 (with errors estimated using variances) and the reduced chi-squared values obtained from the fits are given in Table C1. A comparison of the flat-core and double power law model fits for the full sample based on F-test is given in Table C2. For all the clusters of the sample, except for four, flat-core model is found to provide significantly better fit than the double power law model.

⁵ The flat-core model can also be interpreted as a special case of the double power law model with $K_1 = K_0$, $\alpha_1 = 0$, $K_2 = K_{100}$ and $\alpha_2 = \alpha$.

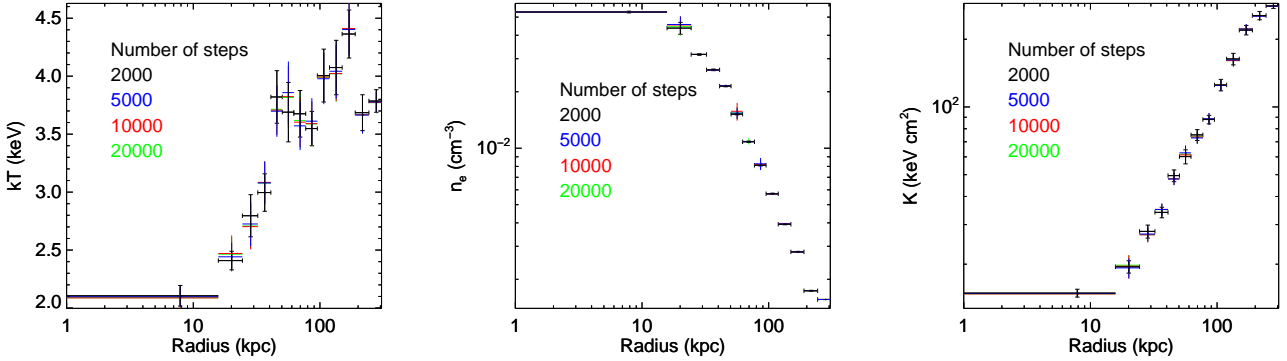


Figure A13. Temperature, electron density and entropy profiles obtained from the jMCMC analysis of the test cluster using 2000 (black), 5000 (blue), 10000 (red) and 20000 (green) steps along each parameter direction in the MCMC random walk.

Table C2. Upper Panel: Comparison of results from single-power law (SPL) and flat-core (FC) models based on F-test for the PL sample. Lower Panel: Comparison of results from flat-core (FC) and double power law (DPL) models based on F-test for the complete sample. F-value is calculated as $F = ((\chi_1^2 - \chi_2^2)/(DOF_1 - DOF_2))/(\chi_2^2/DOF_2)$. The last column gives the probability that model 2 is an improvement over model 1.

Cluster Name	χ_1^2	DOF ₁	χ_2^2	DOF ₂	F-value	Prob. (%)
(SPL)		(FC)				
A85	36.81	9	13.36	8	14.04	99.44
A478	37.10	14	22.23	13	8.70	98.87
A2029	61.75	13	51.84	12	2.29	84.43
A3112	164.16	9	101.92	8	4.89	94.20
(FC)		(DPL)				
A85	13.36	8	44.59	7	-4.90	0.00
A133	19.25	5	20.84	4	-0.31	0.00
A478	22.23	13	28.80	12	-2.73	0.00
A1650	2.12	4	4.05	3	-1.43	0.00
A1795	11.66	11	5.90	10	9.76	98.92
A2029	51.84	12	97.79	11	-5.17	0.00
A2142	3.42	6	7.20	5	-2.63	0.00
A2204	13.36	4	15.72	3	-0.45	0.00
A2244	4.28	4	6.18	3	-0.92	0.00
A2597	9.36	8	11.55	7	-1.32	0.00
A3112	101.92	8	127.68	7	-1.41	0.00
Hydra-A	111.18	6	19.75	5	23.15	99.52
A754	10.70	10	11.79	9	-0.83	0.00
A2256	41.80	5	18.52	4	5.03	91.16
A3158	5.07	3	10.72	2	-1.05	0.00
A3667	22.26	6	24.85	5	-0.52	0.00
ZWCL1215	4.75	5	1.64	4	7.59	94.88

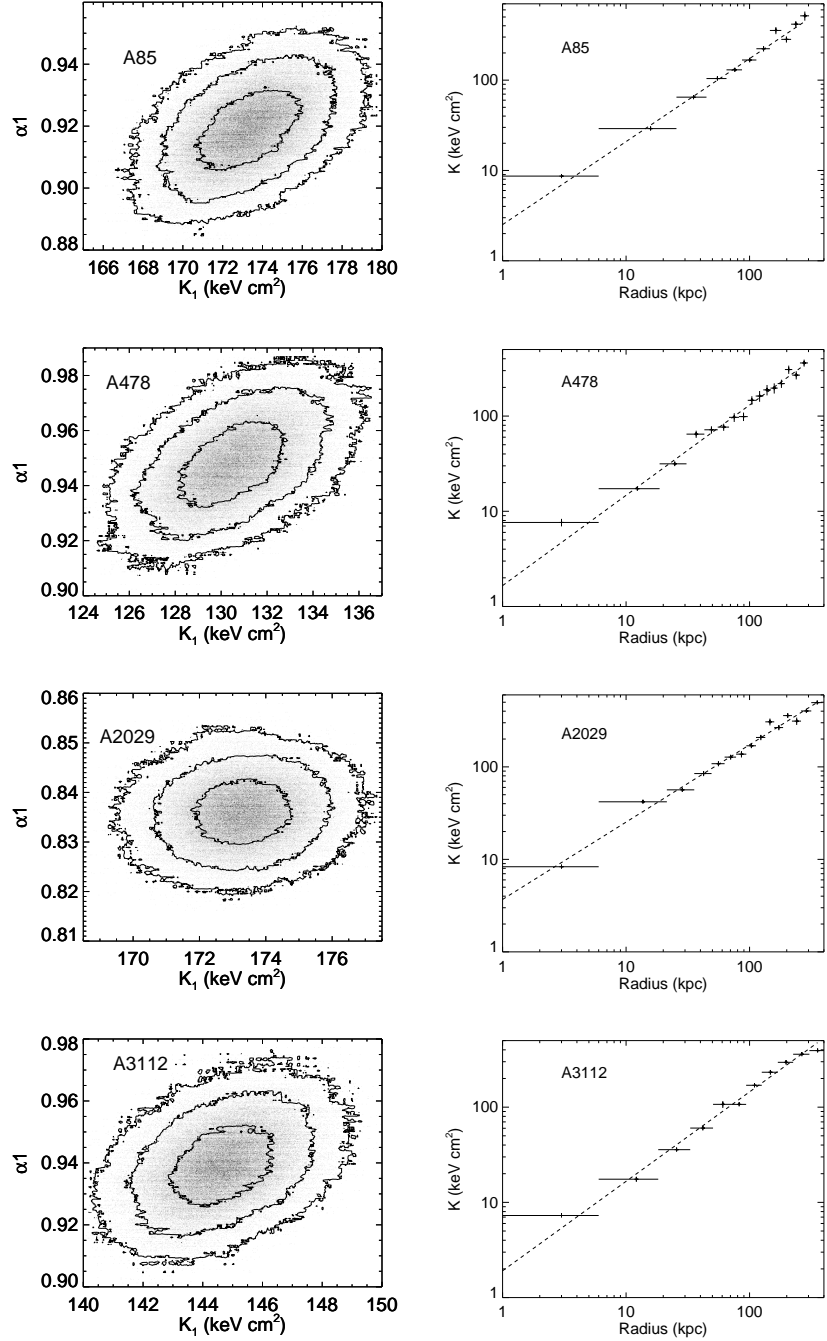


Figure B14. The K_1 - α_1 probability distributions obtained from the single power law entropy model fitting for PL sample. The contours mark the 50%, 90% and 99% inclusion levels based on the density of points starting from the innermost contour outwards. Greyscale denotes the PDF density.

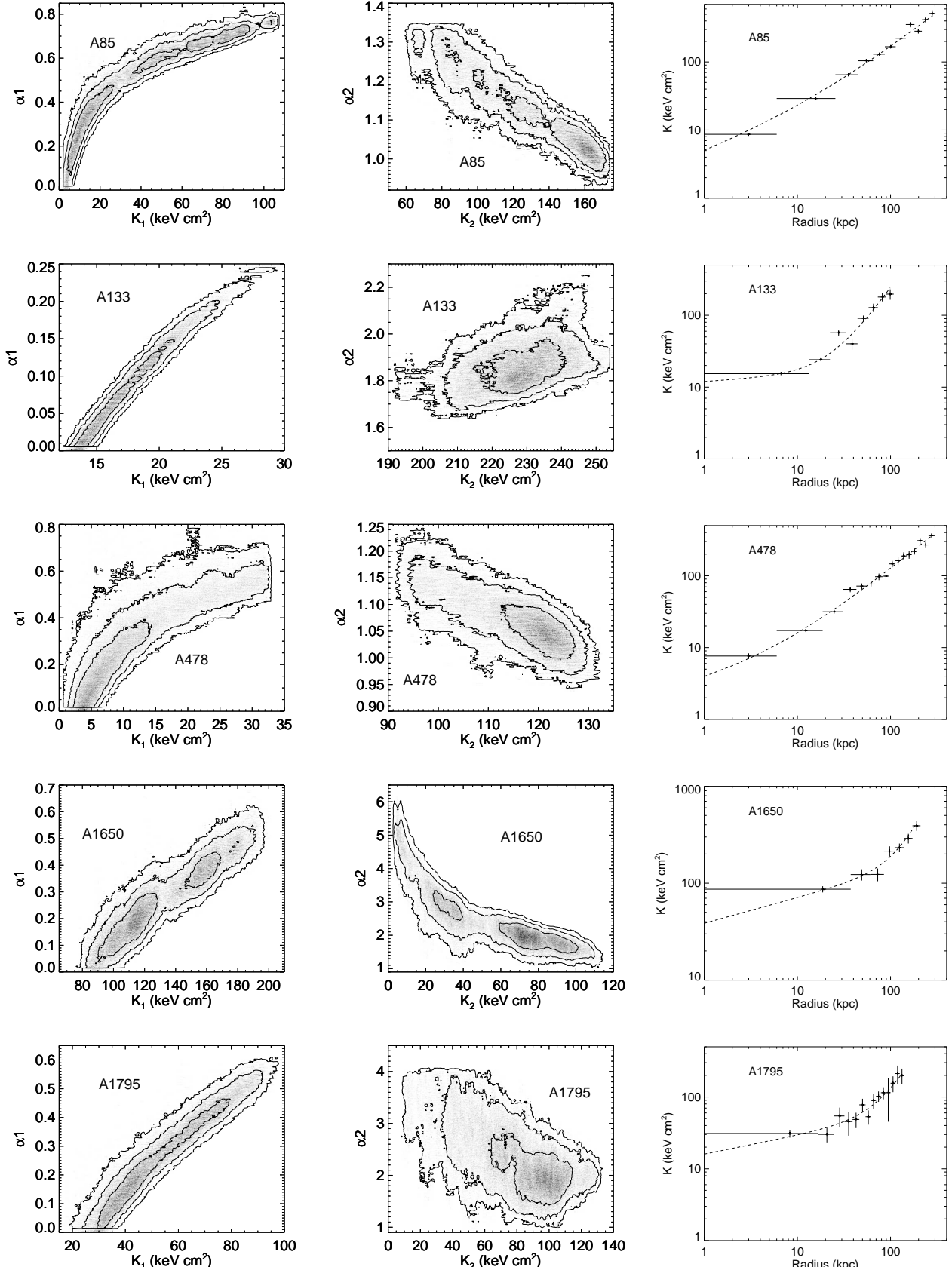


Figure C15. The K_1 - α_1 and K_2 - α_2 marginalized probability distributions obtained from the double power law entropy model fitting for the full cluster sample. The contours mark the 50%, 90% and 99% inclusion levels based on the density of points starting from the innermost contour outwards. Greyscale denotes the PDF density.

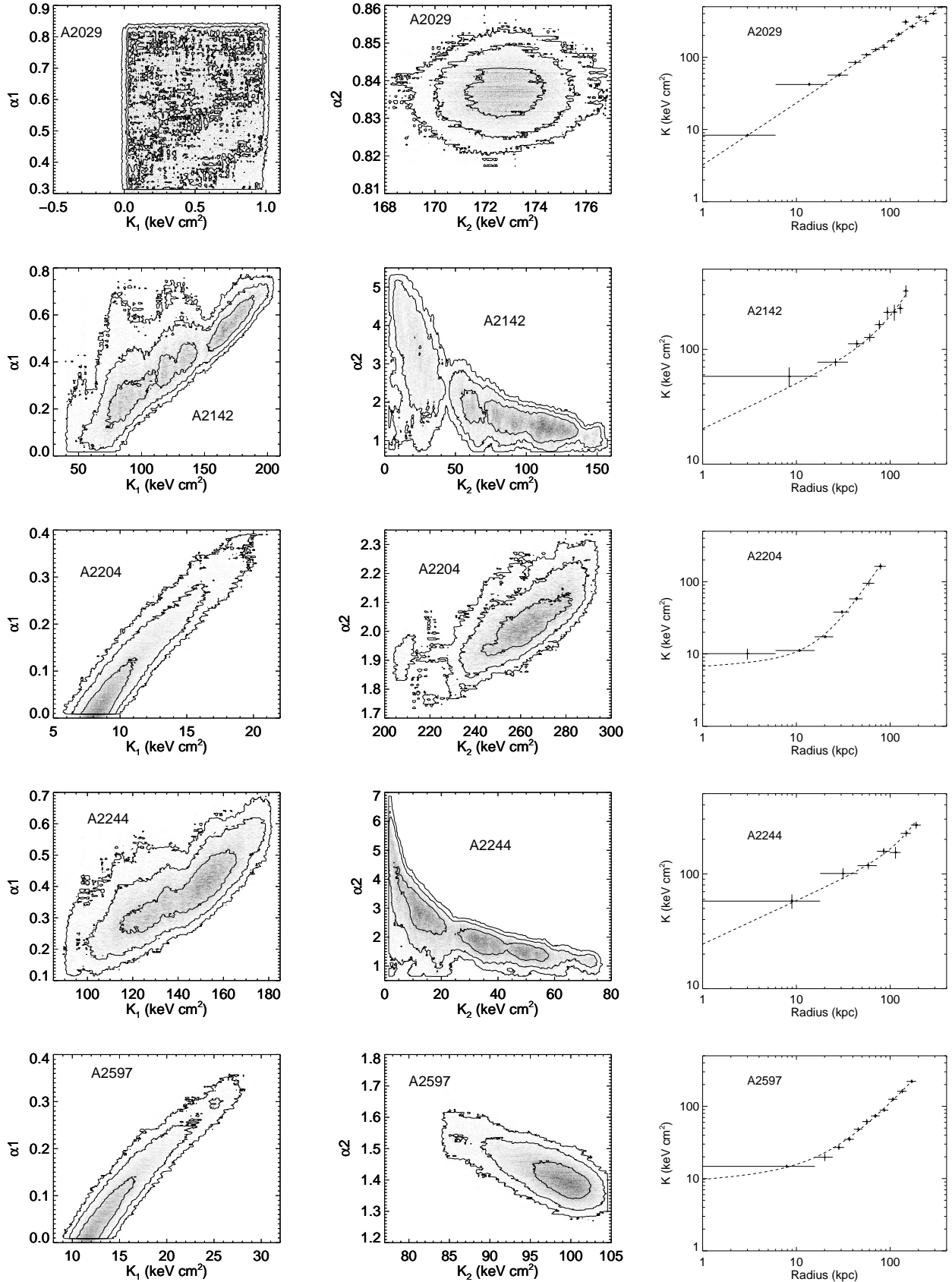


Figure C15. (Contd.)

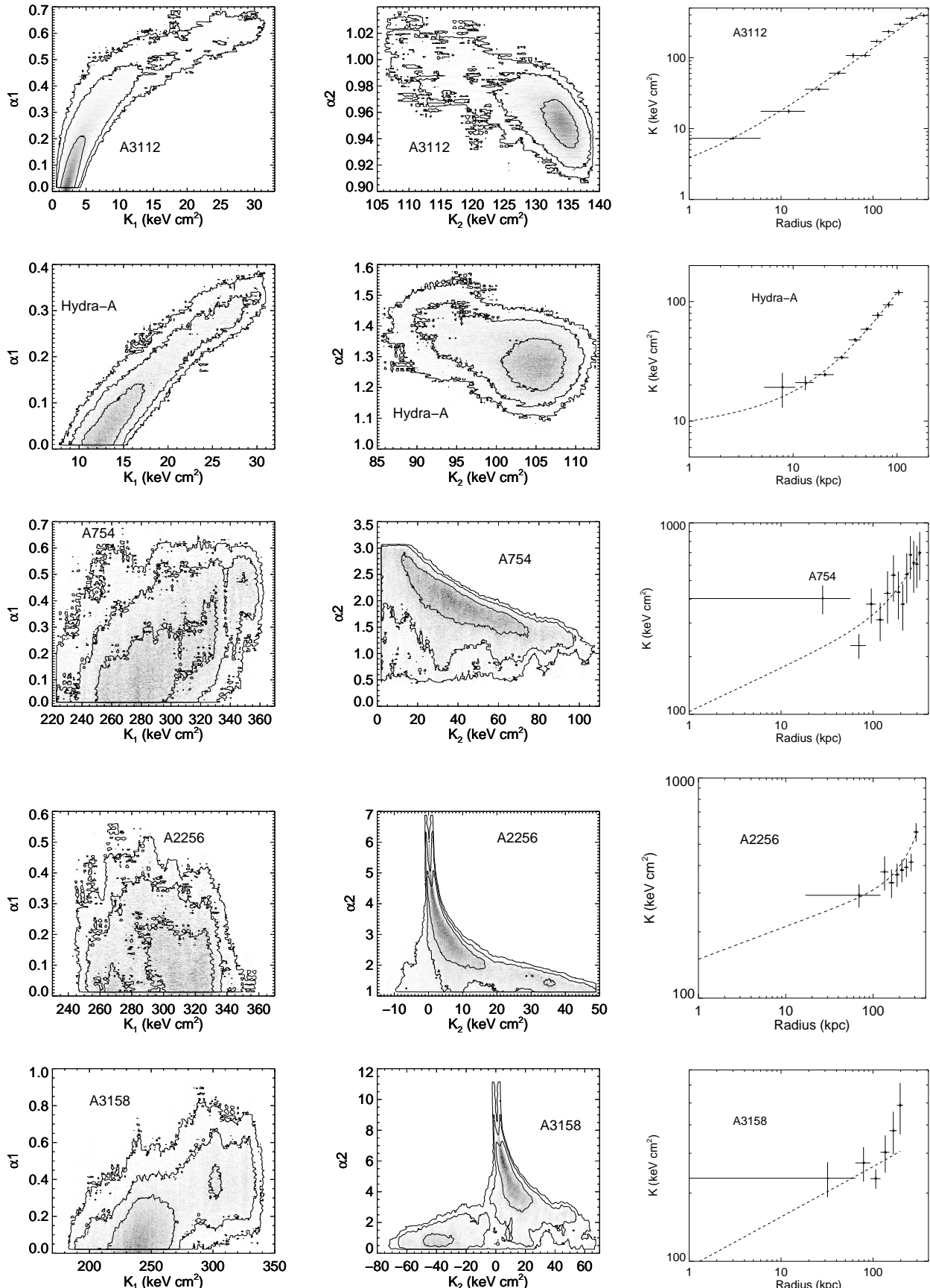


Figure C15. (Contd.)

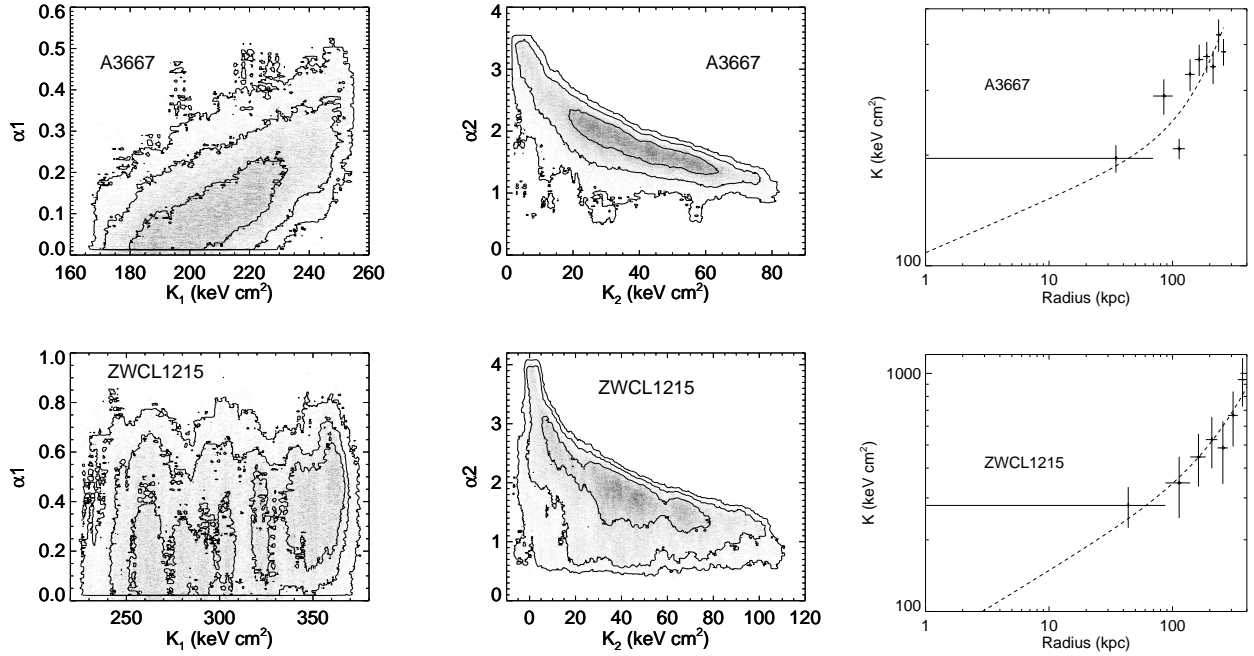


Figure C15. (Contd.)